

# Evaluation of probabilistic photometric redshift estimation approaches for LSST

S.J. Schmidt<sup>1</sup>, A.I. Malz<sup>2,3,4</sup>, J.Y.H. Soo<sup>5</sup>, I.A. Almosallam<sup>6,7</sup>, M. Brescia<sup>8</sup>, S. Cavaudi<sup>8,9</sup>, J. Cohen-Tanugi<sup>10</sup>, A.J. Connolly<sup>11</sup>, P.E. Freeman<sup>12</sup>, M.L. Graham<sup>11</sup>, K. Iyer<sup>13</sup>, M.J. Jarvis<sup>14,15</sup>, J.B. Kalmbach<sup>16</sup>, E. Kovacs<sup>17</sup>, A.B. Lee<sup>12</sup>, G. Longo<sup>9</sup>, C. B. Morrison<sup>11</sup>, J. Newman<sup>18</sup>, E. Nourbakhsh<sup>1</sup>, E. Nuss<sup>10</sup>, T. Pospisil<sup>12</sup>, H. Tranin<sup>10</sup>, R. Zhou<sup>18</sup>, R. Izbicki<sup>19,20</sup>

(LSST Dark Energy Science Collaboration)

<sup>1</sup> Department of Physics, University of California, One Shields Ave., Davis, CA, 95616, USA

<sup>2</sup> German Centre of Cosmological Lensing, Ruhr-Universitaet Bochum, Universitaetsstraße 150, 44801 Bochum, Germany

<sup>3</sup> Center for Cosmology and Particle Physics, New York University, 726 Broadway, New York, 10003, USA

<sup>4</sup> Department of Physics, New York University, 726 Broadway, New York, 10003, USA

<sup>5</sup> Department of Physics and Astronomy, University College London, Gower Street, London WC1E 6BT, UK

<sup>6</sup> King Abdulaziz City for Science and Technology, Riyadh 11442, Saudi Arabia

<sup>7</sup> Information Engineering, Parks Road, Oxford, OX1 3PJ, UK

<sup>8</sup> INAF-Capodimonte Observatory, Salita Moiariello 16, I-80131, Napoli, Italy

<sup>9</sup> Department of Physics E. Pancini, University Federico II, via Cinthia 6, I-80126, Napoli, Italy

<sup>10</sup> Laboratoire Univers et Particules de Montpellier, Université de Montpellier, CNRS, Montpellier, France

<sup>11</sup> Department of Astronomy, University of Washington, Box 351580, U.W., Seattle WA 98195, USA

<sup>12</sup> Department of Statistics & Data Science, Carnegie Mellon University, 5000 Forbes Avenue, Pittsburgh, PA 15213, USA

<sup>13</sup> Department of Physics and Astronomy, Rutgers, The State University of New Jersey, 136 Frelinghuysen Road, Piscataway, NJ 08854-8019 USA

<sup>14</sup> Astrophysics, Department of Physics, University of Oxford, Denys Wilkinson Building, Keble Road, Oxford, OX1 3RH, UK

<sup>15</sup> Department of Physics and Astronomy, University of the Western Cape, Bellville 7535, South Africa

<sup>16</sup> Department of Physics, University of Washington, Box 351560, Seattle, WA 98195, USA

<sup>17</sup> Argonne National Laboratory, Lemont, IL 60439, USA

<sup>18</sup> Department of Physics and Astronomy and the Pittsburgh Particle Physics, Astrophysics and Cosmology Center (PITT PACC), University of Pittsburgh, Pittsburgh, PA 15260, USA

<sup>19</sup> Department of Statistics, Federal University of Sao Carlos, Sao Carlos, Brazil

<sup>20</sup> External collaborator

4 September 2019

## ABSTRACT

Many scientific investigations of photometric galaxy surveys require redshift estimates, whose uncertainty properties are best encapsulated by photometric redshift (photo- $z$ ) posterior probability distribution functions (PDFs). A plethora of photo- $z$  PDF estimation methodologies abound, producing discrepant results with no consensus on a preferred approach. We present the results of a comprehensive experiment comparing twelve photo- $z$  algorithms applied to mock data produced for the Large Synoptic Survey Telescope (LSST) Dark Energy Science Collaboration (DESC). By supplying perfect prior information, in the form of the complete template library and a representative training set as inputs to each code, we demonstrate the impact of the assumptions underlying each technique on the output photo- $z$  PDFs. In the absence of a notion of true, unbiased photo- $z$  PDFs, we evaluate and interpret multiple metrics of the ensemble properties of the derived photo- $z$  PDFs as well as traditional reductions to photo- $z$  point estimates. We report systematic biases and overall over/under-breadth of the photo- $z$  PDFs of many popular codes, which may indicate avenues for improvement in the algorithms or implementations. Furthermore, we raise attention to the limitations of established metrics for assessing photo- $z$  PDF accuracy; though we identify the conditional density estimate (CDE) loss as a promising metric of photo- $z$  PDF performance in the case where true redshifts are available but true photo- $z$  PDFs are not, we emphasize the need for science-specific performance metrics.

**Key words:** galaxies: distances and redshifts – galaxies: statistics – methods: statistical

## 2 LSST Dark Energy Science Collaboration

### 1 INTRODUCTION

The current and next generations of large-scale galaxy surveys, including the Dark Energy Survey (DES, Abbott et al. 2005), the Kilo-Degree Survey (KiDS, de Jong et al. 2013), Hyper Suprime-Cam Survey (HSC, Aihara et al. 2018a,b), Large Synoptic Survey Telescope (LSST, Abell et al. 2009), Euclid (Laureijs et al. 2011), and Wide-Field Infrared Survey Telescope (WFIRST, Green et al. 2012), represent a paradigm shift to reliance on photometric, rather than solely spectroscopic, galaxy catalogues of substantially larger size at a cost of lacking complete spectroscopically confirmed redshifts (z).

Effective astrophysical inference using the catalogues resulting from these ongoing and upcoming missions, however, necessitates accurate and precise photometric redshift (photo-z) estimation methodologies. As an example, in order for photo-z systematics to not dominate the statistical noise floor of LSST’s main cosmological sample of  $\sim 10^7$  galaxies, the LSST Science Requirements Document (SRD)<sup>1</sup> specifies that individual galaxy photo-zs must have root-mean-square error  $\sigma_z < 0.02(1+z)$ ,  $3\sigma$  catastrophic outlier rate below 10%, and bias below 0.003. Specific science cases may have their own requirements on photo-z performance that exceed those of the survey as a whole. In that vein, the LSST Dark Energy Science Collaboration (LSST-DESC) developed a separate SRD (The LSST Dark Energy Science Collaboration et al. 2018) that conservatively forecasts the constraining power of five cosmological probes, leading to even more stringent requirements on photo-z performance, including those defined in terms of tomographically binned subsamples populations rather than individual galaxies.

Though the standard has long been for each galaxy in a photometric catalogue to have a photo-z point estimate and Gaussian error bar, even early applications of photo-zs in precision cosmology indicate the inadequacy of point estimates (Mandelbaum et al. 2008) to encapsulate the degeneracies resulting from the nontrivial mapping between broad band fluxes and redshift. Far from a hypothetical situation, this degeneracy is a real consequence of the same deep imaging that enables larger galaxy catalogue sizes. The lower luminosity and higher redshift populations captured by deeper imaging introduce major physical systematics to photo-zs, among them the Lyman break/Balmer break degeneracy, that did not affect shallower large area surveys like the Sloan Digital Sky Survey (SDSS, York et al. 2000) and Two Micron All Sky Survey (2MASS, Skrutskie et al. 2006).

To fully characterize such physical degeneracies, later photometric galaxy catalogue data releases, (e. g. Sheldon et al. (2012); Erben et al. (2013); de Jong et al. (2017)), provide a more informative photo-z data product, the photo-z probability density function (PDF), that describes the redshift probability, commonly denoted as  $p(z)$ , as a function of a galaxy’s redshift, conditioned on the observed photometry. Early template-based methods such as Fernández-Soto et al. (1999) approximated the likelihood of photometry conditioned on redshift with the relative  $\chi^2$  values of template

spectra. Not long after, Bayesian adaptations of template-based approaches such as Benítez (2000) combined the estimated likelihoods with a prior to yield a posterior PDF of redshift conditioned on photometry. While the first data-driven photo-z algorithms yielded a point estimate, Firth et al. (2003) estimated a photo-z PDF using a neural net with realizations scattered within the photometric errors.

There are numerous techniques for deriving photo-z PDFs, yet no one method has been established as clearly superior. In fact, in the absence of simulated data drawn from known redshift distributions, the very concept of a “true PDF” for an individual galaxy is unavailable, and we must instead rely on measures of ensemble behaviour to characterize PDF quality (see § 4 for further discussion). This caveat aside, quantitative comparisons of photo-z methods have been made before; the Photo-z Accuracy And Testing (PHAT, Hildebrandt et al. 2010) effort focused on photo-z point estimates derived from many photometric bands. Rau et al. (2015) introduced a new method for improving photo-z PDFs using an ordinal classification algorithm. DES compared several codes for photo-z point estimates and a subset with photo-z PDF information (Sánchez et al. 2014) and examined summary statistics of photo-z PDFs for tomographically binned galaxy subsamples (Bonnell et al. 2016).

This paper is distinguished from other comparisons of photo-z methods by its focus on the evaluation criteria for photo-z PDFs and interpretation thereof. We aim to perform a comprehensive sensitivity analysis of photo-z PDF techniques in order to ultimately select those that will become part of the LSST pipelines, as part of a key project of the Photometric Redshifts working group of the LSST-DESC, described in the Science Roadmap (SRM)<sup>2</sup>. In this initial study, we focus on evaluating the performance of photo-z PDF codes using PDF-specific performance metrics in a controlled experiment with complete and representative prior information (template libraries and training sets) to set a baseline for subsequent investigations. This approach probes how each code considered exploits the information content of the data versus prior information from template libraries and training sets.

The outline of the paper is as follows: in § 2 we present the simulated data set; in § 3 we describe the current generation codes employed in the paper; in § 4 we discuss the interpretation of photo-z PDFs in terms of metrics of accuracy; in § 5 we show our results and compare the performance of the codes; in § 6 we offer our conclusions and discuss future extensions of this work.

### 2 DATA

In order to test the current generation of photo-z PDF codes, we employ an existing simulated galaxy catalogue, described in detail in Section 2.1. The experimental conditions shared among all codes are motivated by the LSST SRD requirements and implemented for machine learning and template-based photo-z PDF codes according to the procedures of Sections 2.3.1 and 2.3.2 respectively.

<sup>1</sup> available at <https://docushare.lsstcorp.org/docushare/dsweb/Get/LPM-17>

<sup>2</sup> Available at: [http://lsst-desc.org/sites/default/files/DESC\\_SRMs\\_V1\\_1.pdf](http://lsst-desc.org/sites/default/files/DESC_SRMs_V1_1.pdf)

113 **2.1 The Buzzard-v1.0 simulation**

114 Our mock catalogue is derived from the BUZZARD-highres-  
 115 v1.0 catalogue (DeRose et al. 2019, Wechsler et al., in prep).  
 116 BUZZARD is built on a dark matter-only N-body simulation  
 117 of  $2048^3$  particles in a  $400 \text{ Mpc h}^{-1}$  box. The lightcone was  
 118 constructed from smoothing and interpolation between a set  
 119 of time snapshots. Dark matter halos were identified using  
 120 the Rockstar software package (Behroozi et al. 2013) and  
 121 then populated with galaxies with a stellar mass and ab-  
 122 solute  $r$ -band magnitude in the SDSS system determined  
 123 using a sub-halo abundance matching model constrained to  
 124 match both projected two-point galaxy clustering statistics  
 125 and an observed conditional stellar mass function (Reddick  
 126 et al. 2013).

127 To assign a spectrum to each galaxy, the Adding Den-  
 128 sity Dependent Spectral Energy Distributions (SEDs) pro-  
 129 cedure (ADDSEDS, deRose in prep.)<sup>3</sup> was used. ADDSEDS uses  
 130 a sample of  $\sim 5 \times 10^5$  galaxies from the magnitude-limited  
 131 SDSS Data Release 6 Value Added Galaxy Catalogue (Blan-  
 132 ton et al. 2005) to train an empirical relation between abso-  
 133 lute  $r$ -band magnitude, local galaxy density, and SED. Each  
 134 SDSS spectrum is parameterized by five weights correspond-  
 135 ing to a weighted sum of five basis SED components using  
 136 the k-correct software package<sup>4</sup> (Blanton & Roweis 2007).

137 Correlations between SED and galaxy environment  
 138 were included so as to preserve the colour-density relation of  
 139 galaxy environment. The distance to the spatially projected  
 140 fifth-nearest neighbour was used as a proxy for local density  
 141 in the SDSS training sample. For each simulated galaxy,  
 142 a galaxy with similar absolute  $r$ -band magnitude and local  
 143 galaxy density was chosen from the training set, and that  
 144 training galaxy's SED was assigned to the simulated galaxy.  
 145 In Section 2.1.1, we discuss the limited realism of this mock  
 146 data.

147 **2.1.1 Caveats**

148 By necessity, BUZZARD does not contain all of the compli-  
 149 cating factors present in real data, and here we discuss the  
 150 most pertinent ways that these limitations affect our exper-  
 151 iment. BUZZARD includes only galaxies, not stars nor AGN.  
 152 The catalogue-based construction excludes image-level ef-  
 153 fects, such as deblending errors, photometric measurement  
 154 issues, contamination from sky background (Zodiacal light,  
 155 scattered light, etc.), lensing magnification, and Galactic  
 156 reddening.

157 The BUZZARD SEDs are drawn from a set of  $\sim 5 \times 10^5$   
 158 SEDs, which themselves are derived from a five-component  
 159 linear combination fit to  $\sim 5 \times 10^5$  SDSS galaxies; thus the  
 160 sample contains only galaxies that resemble linear combina-  
 161 tions of those for which SDSS obtained spectra, and there  
 162 are necessarily duplicates. The linear combination SEDs also  
 163 restrict the properties of the galaxy population to linear  
 164 combinations of the properties corresponding to five basis  
 165 templates, precluding the modeling of non-linear features  
 166 such as the full range of emission line fluxes relative to the  
 167 continuum. The only form of intrinsic dust reddening comes  
 168 from what is already present in the five basis SEDs via the

169 training set used to create the basis templates, and linear  
 170 combinations thereof do not span the full range of realistic  
 171 dust extinction observed in galaxy populations.

172 While these idealized conditions limit the realism of our  
 173 mock data, they are irrelevant to the controlled experimental  
 174 conditions of this study, if anything assuring that differentia-  
 175 tion in the performance of the photo-z PDF codes is due to  
 176 the inferential techniques rather than nuances in the data.

177 **2.2 LSST-like mock observations**

178 Given the SED, absolute  $r$ -band magnitude, and redshift,  
 179 we computed apparent magnitudes in the six LSST filter  
 180 passbands,  $ugrizy$ . We assigned magnitude errors in the six  
 181 bands using the simple model of Ivezić et al. (2008), assum-  
 182 ing achievement of the full 10-year depth, with a modifica-  
 183 tion of fiducial LSST total numbers of 30-second visits for  
 184 photometric error generation: we assume 60 visits in  $u$ -band,  
 185 80 visits in  $g$ -band, 180 visits in  $r$ -band, 180 visits in  $i$ -band,  
 186 160 visits in  $z$ -band, and 160 visits in  $y$ -band.

187 As a consequence of adding Gaussian-distributed pho-  
 188 tometry errors, 2.0% of our galaxies exhibit a negative flux  
 189 in one or more bands, the vast majority of which are in the  
 190  $u$ -band. We deem such negative fluxes *non-detections* and  
 191 assign a placeholder magnitude of 99.0 in the catalogue to  
 192 indicate to the photo-z PDF codes that such galaxies would  
 193 be “looked at but not seen” in multi-band forced photome-  
 194 try.

195 The full dataset thus covers 400 square degrees and con-  
 196 tains 238 million galaxies of redshift  $0 < z \leq 8.7$  down  
 197 to  $r = 29$ . Systematic inconsistencies with galaxy colors  
 198 at  $z > 2$  were observed, so the catalogue was limited to  
 199  $0 < z \leq 2.0$ . To obtain a catalogue matching the LSST  
 200 Gold Sample, we imposed an cut of  $i < 25.3$ , which gives a  
 201 signal-to-noise ratio  $\gtrsim 30$  for most galaxies. In order for sta-  
 202 tistical errors to be subdominant to the systematic errors we  
 203 aim to probe, we further reduced the sample size to  $< 10^7$   
 204 galaxies by isolating  $\sim 16.8$  square degrees selected from five  
 205 separate spatial regions of the simulation. We refer to this  
 206 final set of galaxies as DC1, for the first LSST-DESC Data  
 207 Challenge.

208 **2.3 Shared prior information**

209 For the purpose of performing a controlled experiment that  
 210 compares photo-z PDF codes on equal footing as a baseline  
 211 for a future sensitivity analysis, we take care to provide each  
 212 with maximally optimistic prior information. Redshift esti-  
 213 mation approaches built upon physical modeling and ma-  
 214 chine learning alike have a notion of prior information con-  
 215 sidered beyond the photometry of the data for which redshift  
 216 is to be constrained: that information is derived from a tem-  
 217 plate library for a model-based code and a training set for  
 218 a data-driven code. In this initial study, we seek to set a  
 219 baseline for a later comparison of the performance of photo-  
 220 z PDF codes under incomplete and non-representative prior  
 221 information that will propagate differently in the space of  
 222 data-driven and model-based algorithms. However, for the  
 223 baseline case of perfect prior information, physical model-  
 224 ing and machine learning codes can indeed be put on truly  
 225 equal footing. We outline the equivalent ways of providing  
 226 all codes perfect prior information below.

<sup>3</sup> <https://github.com/vipasu/addsed>

<sup>4</sup> <http://kcorrect.org>

## 4 LSST Dark Energy Science Collaboration

### 227 2.3.1 Training and test set division

228 Following the findings of Bernstein & Huterer (2010), Masters et al. (2017) that only  $10^4$  spectra are necessary to  
 229 calibrate photo- $z$ s to Stage IV requirements, we aimed to  
 230 set aside a randomly selected training set of  $3 - 5 \times 10^4$   
 231 galaxies,  $\sim 10\%$  of the full sample. After all cuts described  
 232 above, we designated the *DC1 training set* of 44 404 galaxies  
 233 for which observed photometry, true SEDs, and true red-  
 234 shifts would be provided to all codes and the blinded  
 235 *DC1 test set* of 399 356 galaxies for which photometry alone  
 236 would be provided to all codes and photo- $z$  PDFs would be  
 237 requested. The exact form of LSST photometric filter trans-  
 238 mission curves were also considered public information that  
 239 could be used by any code.

### 241 2.3.2 Template library construction

242 We aimed to provide template-fitting codes with complete  
 243 yet manageable library of templates spanning the space of  
 244 SEDs of the DC1 galaxies. We constructed  $K = 100$  repre-  
 245 sentative templates from the  $\sim 5 \times 10^5$  SEDs of the SDSS  
 246 DR6 NYU-VAGC by using the five-dimensional vectors of  
 247 SED weight coefficients described above. After regularizing  
 248 the SED weight coefficients  $\in [0, 1]$ , we ran a simple K-means  
 249 clustering algorithm on the five-dimensional space of regu-  
 250 larized SED weight coefficients of the SDSS galaxy sample.  
 251 The resulting clusters were used to define Voronoi cells in  
 252 the space of weight coefficients, with centre positions cor-  
 253 responding to weights for the k-correct SED components,  
 254 yielding the 100 SEDs that comprise the *DC1 template set*  
 255 provided to all template-based codes. We did not, however,  
 256 exclude from consideration template-based codes that made  
 257 modifications in their use of these templates due to archi-  
 258 tecture limitations (as opposed to knowledge of the exper-  
 259 imental conditions that could artificially boost the code's  
 260 apparent performance), with deviations noted in Section 3.

## 261 3 METHODS

262 Here we summarize the twelve photo- $z$  PDF codes compared  
 263 in this study, also in Table 1, which include both estab-  
 264 lished and emerging approaches in template fitting and  
 265 machine learning. Though not exhaustive, this sample rep-  
 266 presents codes for which there was sufficient expertise within  
 267 the LSST-DESC Photometric Redshifts Working Group.  
 268 Some aspects of data treatment were left to the individual  
 269 code runners, for example, whether/how to split the avail-  
 270 able data with known redshifts into separate training and  
 271 validation sets.

272 Another key difference is the treatment of non-  
 273 detections in one or more bands: some codes ignore incom-  
 274 plete bands, while others replace the value with either an  
 275 estimate for the detection limit, the mean of other values in  
 276 the training set, or another default value. There are varying  
 277 conventions among machine learning based codes for treat-  
 278 ment of non-detections, and no one prescription dominates  
 279 in the photo- $z$  literature. The specific choices for each code  
 280 affect the results and contribute to the implicit prior influ-  
 281 encing their output. However, we remind the reader that  
 282 only 2.0 per cent of our sample has non-detections, almost

283 exclusively in the  $u$ -band, and thus should not dominate the  
 284 code performance differences. The authors welcome interest  
 285 from those outside LSST-DESC to have their codes assessed  
 286 in future investigations that build upon this one.

287 We describe the algorithms and implementations of the  
 288 model-based and data-driven codes in Sections 3.1 and 3.2  
 289 respectively, with a straw-person approach included in Sec-  
 290 tion 3.3.

### 291 3.1 Template-based Approaches

292 We test three publicly available and commonly used  
 293 template-based codes that share the standard physically moti-  
 294 vated approach of calculating model fluxes for a set of tem-  
 295 plate SEDs on a grid of redshift values and evaluating a  $\chi^2$   
 296 merit function using the observed and model fluxes:

$$297 \chi^2(z, T, A) = \sum_i^{N_{\text{filt}}} \left( \frac{F_{\text{obs}}^i - A F_{\text{pred}}^i(T, z)}{\sigma_{\text{obs}}^i} \right)^2 \quad (1)$$

298 where  $A$  is a normalization factor,  $F_{\text{pred}}^i(T, z)$  is the flux pre-  
 299 dicted for a template  $T$  at redshift  $z$ ,  $F_{\text{obs}}^i$  is the observed flux  
 300 in a given band  $i$ ,  $\sigma_{\text{obs}}^i$  is the observed flux error, and  $N_{\text{filt}}$  is  
 301 the total number of filters, in our case the six *ugrizy* LSST  
 302 filters. In words, the likelihood is a sum of observed flux er-  
 303 ror  $\sigma_b^{\text{obs}}$ -weighted squared differences between the observed  
 304 flux  $F_b^{\text{obs}}$  and the normalized predicted flux  $F_b^{\text{mod}}(T, z)$  in  
 305  $N_{\text{filt}}$  photometric filters  $b$ , which is the LSST *ugrizy* filters  
 306 in this case. Specific implementation details of each code,  
 307 e. g. prior form and implementation, are described below.

#### 308 3.1.1 BPZ

309 Bayesian Photometric Redshift (**BPZ**<sup>5</sup>, Benítez 2000) de-  
 310 termines the likelihood  $p(C|z, T)$  of a galaxy's observed  
 311 colours  $C$  for a set of SED templates  $T$  at redshifts  
 312  $z$ . The **BPZ** likelihood is related to the  $\chi^2$  likelihood by  
 313  $p(C|z, T) \propto \exp[-\chi^2/2]$ . Given a Bayesian prior  $p(z, T|m_0)$   
 314 over apparent magnitude  $m_0$  and type  $T$ , and assuming  
 315 that the SED templates are spanning and exclusive, **BPZ**  
 316 constructs the redshift posterior  $p(z|C, m_0)$  by marginaliz-  
 317 ing over all SED templates with the form  $p(z|C, m_0) \propto$   
 318  $\sum_T p(C|z, T) p(z, T|m_0)$  (Eq. 3 from Benítez 2000), corre-  
 319 sponding to setting the parameter `PROBS_LITE=TRUE` in the  
 320 **BPZ** parameter file. The **BPZ** prior is the product of an SED  
 321 template proportion that varies with apparent magnitude  
 322  $p(T|m_0)$  and a prior  $p(z|T, m_0)$  over the expected redshift as  
 323 a function of apparent magnitude and SED template. We an-  
 324 ticipate **BPZ** to outperform other template-based approaches  
 325 due to the prior that both comprehensively accounts for SED  
 326 type and is calibrated to the training set.

327 Here we test **BPZ**-v 1.99.3 (Benítez 2000) with the DC1  
 328 template set of Section 2.3.2. To keep the number of free pa-  
 329 rameters manageable, the DC1 template set is pre-sorted by  
 330 the rest-frame  $u - g$  colour and split into three broad classes  
 331 of SED template, equivalent to the E, Sp and Im/SB types.  
 332 The Bayesian prior term  $p(T|m_0)$  was derived directly from  
 333 the DC1 training set, and the other term  $p(z|T, m_0)$  was  
 334 chosen to be the best fit for the eleven free parameters from

5 <http://www.stsci.edu/~dcoe/BPZ/>

**Table 1.** List of photo-z PDF codes featured in this study

Published code	Type	Public source code
LePhare (Arnouts et al. 1999)	template fitting	<a href="http://www.cfht.hawaii.edu/~arnouts/lephare.html">http://www.cfht.hawaii.edu/~arnouts/lephare.html</a>
BPZ (Benítez 2000)	template fitting	<a href="http://www.stsci.edu/~dcoe/BPZ/">http://www.stsci.edu/~dcoe/BPZ/</a>
EAZY (Brammer et al. 2008)	template fitting	<a href="https://github.com/gbrammer/eazy-photoz">https://github.com/gbrammer/eazy-photoz</a>
ANNz2 (Sadeh et al. 2016)	machine learning	<a href="https://github.com/IftachSadeh/ANNZ">https://github.com/IftachSadeh/ANNZ</a>
FlexZBoost (Izbicki & Lee 2017)	machine learning	<a href="https://github.com/tospisic/flexcode">https://github.com/tospisic/flexcode</a> ; <a href="https://github.com/rizbicki/FlexCoDE">https://github.com/rizbicki/FlexCoDE</a>
GPz (Almosallam et al. 2016b)	machine learning	<a href="https://github.com/OxfordML/GPz">https://github.com/OxfordML/GPz</a>
METAPhoR (Cavuoti et al. 2017)	machine learning	<a href="http://dame.dsf.unina.it">http://dame.dsf.unina.it</a>
CMNN (Graham et al. 2018)	machine learning	N/A
SkyNet (Graff et al. 2014)	machine learning	<a href="http://ccforge.cse.rl.ac.uk/gf/project/skynet/">http://ccforge.cse.rl.ac.uk/gf/project/skynet/</a>
TPZ (Carrasco Kind & Brunner 2013)	machine learning	<a href="https://github.com/mgckind/MLZ">https://github.com/mgckind/MLZ</a>
Delight (Leistedt & Hogg 2017)	hybrid	<a href="https://github.com/ixkael/Delight">https://github.com/ixkael/Delight</a>
trainZ	machine learning	See Section 3.3

335 the functional form of Benítez (2000). We use template interpolation, creating two linearly interpolated templates between each basis SED (sorted by rest-frame  $u - g$  colour) by setting the parameter `INTERP=2`. Prior to running the code, the non-detection placeholder magnitude was replaced with an estimate of the one- $\sigma$  detection limit for the undetected band as a proxy for a value close to the estimated sky noise threshold.

### 3.1.2 EAZY

344 Easy and Accurate Photometric Redshifts from Yale (EAZY<sup>6</sup>,  
345 Brammer et al. 2008) extends the basic  $\chi^2$  fit procedure that  
346 defines template-fitting approaches. The algorithm models  
347 the observed photometry with a linear combination of tem-  
348 plate SEDs at each redshift. The best-fit SED at each red-  
349 shift is found by simultaneously fitting one, two, or all of  
350 the templates via  $\chi^2$  minimization, which is distinct from  
351 marginalizing across all templates. The minimized  $\chi^2$  like-  
352 lihood at each redshift is then combined with an apparent  
353 magnitude prior to obtain the redshift posterior PDF. We  
354 note that the utilization of the best-fit SED conditioned on  
355 redshift rather than a proper marginalization does not lead  
356 to the correct posterior distribution, an implementation is-  
357 sue that has now been identified and will be addressed by  
358 the developers in the future.

359 In contrast with BPZ, EAZY’s apparent magnitude prior is  
360 independent of SED, though it was derived empirically from  
361 the DC1 training set. The EAZY architecture cannot accept  
362 a template set other than the same five basis templates em-  
363 ployed by `k-correct` when constructing the DC1 catalogue,  
364 but, for consistency with the experimental scope of perfect  
365 prior information, EAZY’s flexible `all-templates` mode was  
366 used to fit the photometric data with a linear combination  
367 of the five basis templates. Though EAZY can account for  
368 uncertainty in the template set by adding in quadrature to  
369 the flux errors an empirically derived template error as a  
370 function of redshift, we set the template error to zero since  
371 the same templates were in fact used to produce the DC1  
372 photometry.

### 3.1.3 LePhare

373 Photometric Analysis for Redshift Estimate (LePhare<sup>7</sup>,  
374 Arnouts et al. 1999; Ilbert et al. 2006) uses the  $\chi^2$  of Equation 1 to match observed colors with those predicted from  
375 a template set, which can be semi-empirical or entirely syn-  
376 synthetic, directly according to the The reported photo-z PDF  
377 is an arbitrary normalization of the likelihood evaluated on  
378 the output redshift grid.

379 Here we use LePhare-v 2.2 with the DC1 template set  
380 of Section 2.3.2. Unlike both BPZ and EAZY, LePhare uses  
381 generic, SED-independent priors that are not tuned to the  
382 DC1 data set.

## 3.2 Machine Learning-based Approaches

383 We compared nine data-driven photo-z estimation ap-  
384 proaches, eight of which are described in this section and one  
385 of which is discussed in Section 3.3. Because the algorithms  
386 differ more from one another and the techniques are rela-  
387 tive newcomers to the astronomical literature, we provide  
388 somewhat more detail about the implementations below.

### 3.2.1 ANNz2

389 ANNz2<sup>8</sup> (Sadeh et al. 2016) supports several machine learn-  
390 ing algorithms, including artificial neural networks (ANN),  
391 boosted decision tree, and k-nearest neighbour (KNN) re-  
392 gression. In addition to accounting for errors on the input  
393 photometry, ANNz2 uses the KNN-uncertainty estimate of  
394 Oyaizu et al. (2008) to quantify uncertainty in the choice of  
395 method over multiple runs. Using the Toolkit for Multivariate  
396 Data Analysis with ROOT<sup>9</sup>, ANNz2 can return the results  
397 of running a single machine learning algorithm, a “best”  
398 choice of the results from simultaneously running multiple  
399 algorithms (based on evaluation the cumulative distribution  
400 functions of validation set objects), or a combination of the  
401 results of multiple algorithms weighted by their method un-  
402 certainties averaged over multiple runs.

403 In this study, we used ANNz2-v.2.0.4 to output only the  
404 result of the ANN algorithm. Photo-z PDFs were produced  
405 by running an ensemble of 5 ANNs with a 6 : 12 : 12 : 1

<sup>6</sup> <https://github.com/gbrammer/eazy-photoz>

<sup>7</sup> <http://www.cfht.hawaii.edu/~arnouts/lephare.html>

<sup>8</sup> <https://github.com/IftachSadeh/ANNZ>

<sup>9</sup> <http://tmva.sourceforge.net/>

## 6 LSST Dark Energy Science Collaboration

410 architecture corresponding to the 6 *ugrizy* inputs, 2 hidden  
 411 layers with 12 nodes each, and 1 output of redshift. Each of  
 412 the five ANNs was trained with different random seeds for  
 413 the initialization of input parameters, reserving half of the  
 414 training set for validation to prevent overfitting. Undetected  
 415 galaxies were excluded from the training set, and per-band  
 416 non-detections in the test set were replaced with the mean  
 417 magnitude in that band within the entire test set.

### 418 3.2.2 Colour-Matched Nearest-Neighbours

419 The colour-matched nearest-neighbours photometric red-  
 420 shift estimator (CMNN, Graham et al. 2018) uses a training  
 421 set of galaxies with known redshifts that has equivalent or  
 422 better photometry than the test set in terms of quality and  
 423 filter coverage. For each galaxy in the test set, CMNN identifies  
 424 a colour-matched subset of training galaxies using a thresh-  
 425 old in the Mahalanobis distance  $D_M = \sum_j^{N_{\text{colours}}} (c_j^{\text{train}} -$   
 426  $c_j^{\text{test}})^2 / \delta c_{\text{test}}^2$  in the space of available colours  $c$ , with colour  
 427 measurement errors  $\delta c_{\text{test}}$  and  $N_{\text{colours}} = 5$  colors  $j$  defined  
 428 by the *ugrizy* filters, which defines the set of colour-matched  
 429 neighbours based on a value of the percent point function  
 430 (PPF). As an example, for  $N_{\text{filt}} = 5$  with PPF= 0.95, 95%  
 431 of all training galaxies consistent with the test galaxy will  
 432 have  $D_M < 11.07$ . Undetected bands are dropped, thereby  
 433 reducing the effective  $N_{\text{filt}}$  for that galaxy. The photo- $z$  PDF  
 434 of a given test set galaxy is the normalized distribution of  
 435 redshifts of its colour-matched subset of training set galax-  
 436 ies.

437 Here, we make two modifications to the implementation  
 438 of Graham et al. (2018) to comply with the controlled exper-  
 439 imental conditions. First, we do not impose non-detections  
 440 on galaxies fainter than the expected LSST 10-year limit-  
 441 ing magnitude nor galaxies bright enough to saturate with  
 442 LSST’s CCDs, instead using all of the photometry for the  
 443 DC1 test and training sets. Second, we apply the initial  
 444 colour cut to the training set before calculating the Ma-  
 445 halanobis distance in order to accelerate processing and use a  
 446 magnitude pseudo-prior as in Graham et al. (2018), but for  
 447 both we use cut-off values corresponding to the DC1 training  
 448 set galaxies’ colours and magnitudes.

449 We make an additional adaptation to enable the CMNN  
 450 algorithm to yield accurate photo- $z$  PDFs for all galaxies,  
 451 as the original Graham et al. (2018) algorithm is optimized  
 452 for photo- $z$  point estimates and is susceptible to less ac-  
 453 curate photo- $z$  PDFs for bright galaxies or those with few  
 454 matches in colour-space. We use PPF= 0.95 rather than  
 455 PPF= 0.68 to generate the subset of colour-matched train-  
 456 ing galaxies, whose redshifts are weighted by their inverse  
 457 Mahalanobis distances of the when composing the photo-  
 458  $z$  PDF rather than weighting all colour-matched training  
 459 galaxies equally. Additionally, when the number of colour-  
 460 matched training set galaxies is less than 20, the nearest 20  
 461 neighbours in color-space are used instead, and the output  
 462 photo- $z$  PDF is convolved with a Gaussian kernel of vari-  
 463 ance  $\sigma_{\text{train}}^2 (\text{PPF}_{20}/0.95)^2 - 1$  to account for the correspond-  
 464 ing growth of the effective PPF to include 20 neighbors.

### 465 3.2.3 Delight

466 **Delight**<sup>10</sup> (Leistedt & Hogg 2017) is a hybrid technique that  
 467 infers photo- $z$ s with a data-driven model of latent SEDs and  
 468 a physical model of photometric fluxes as a function of red-  
 469 shift. Generally, machine learning methods rely on represen-  
 470 tative training data with shared photometric filters, while  
 471 template based methods rely on a complete library of tem-  
 472 plates based on physical models constructed. **Delight** aims  
 473 to take the best aspects of both approaches by construct-  
 474 ing a large collection of latent SED templates (or physical  
 475 flux-redshift models) from training data, with a template  
 476 SED library as a guide to the learning of the model, thereby  
 477 circumventing the machine learning prerequisite of represen-  
 478 tative training data in the same photometric bands and the  
 479 template fitting requirement of detailed galaxy SED models.  
 480 It models noisy observed flux  $\hat{\mathbf{F}} = \mathbf{F} + F_b$  as a sum of a noise-  
 481 less flux plus a Gaussian processes  $F_b \sim \mathcal{GP}(\mu^F, k^F)$  with  
 482 zero mean function  $\mu^F$  and a physically motivated kernel  $k^F$   
 483 that induces realistic correlations in flux-redshift space.

484 From a template-fitting perspective, each test set galaxy  
 485 has a posterior  $p(z|\hat{\mathbf{F}}) \approx \sum_i p(\hat{\mathbf{F}}|z, T_i)p(z|T_i)p(T_i)$  of red-  
 486 shift  $z$  conditioned on noisy flux  $\hat{\mathbf{F}}$ , where  $p(z|T_i)p(T_i)$  cap-  
 487 tures prior information about the redshift distributions and  
 488 abundances of the galaxy templates  $T_i$ . As in traditional  
 489 template fitting, each likelihood  $p(\hat{\mathbf{F}}|\mathbf{F})$  relates the noisy flux  
 490  $\hat{\mathbf{F}}$  with the noiseless flux  $\mathbf{F}$  predicted by the model of a linear  
 491 combination of templates, carefully constructed to account  
 492 for model uncertainties and different normalization of the  
 493 same SED, plus the Gaussian process term.

494 The machine learning approach appears in the inclu-  
 495 sion of a pairwise comparison term  $p(\mathbf{F}|z, z_j, \hat{\mathbf{F}}_j)$  for the  
 496 prediction of model flux  $\mathbf{F}$  at a model redshift  $z$  with re-  
 497 spect to training set galaxy  $j$  with redshift  $z_j$  and ob-  
 498 served flux  $\hat{\mathbf{F}}_j$ . Thus the photo- $z$  posterior  $p(\hat{\mathbf{F}}|z, T_i) =$   
 499  $\int p(\hat{\mathbf{F}}|\mathbf{F})p(\mathbf{F}|z, z_j, \hat{\mathbf{F}}_j)d\mathbf{F}$  may be interpreted as the proba-  
 500 bility that the training and the target galaxies have the same  
 501 SED at different redshifts. The flux prediction  $p(\mathbf{F}|z, z_j, \hat{\mathbf{F}}_j)$   
 502 of the training galaxy at redshift  $z$  is modeled via the Gaus-  
 503 sian process described above; more detail is provided in  
 504 Leistedt & Hogg (2017).

505 In this study, the default settings of **Delight** were used,  
 506 with the exception that the PDF bins were set to be linearly-  
 507 spaced rather than logarithmic. The Gaussian process was  
 508 trained using the full DC1 training set. We used the full DC1  
 509 template set with a flat prior in magnitude and SED type.  
 510 Photometric uncertainties from the inputs are propagated  
 511 into the code, while non-detections for each band are set to  
 512 the mean of the respective bands.

### 513 3.2.4 FlexZBoost

514 **FlexZBoost**<sup>11</sup> (Izbicki & Lee 2017) is built on **FlexCode**, a  
 515 general-purpose methodology for converting any conditional  
 516 mean point estimator of  $z$  to a conditional density estima-  
 517 tor  $p(z|\mathbf{x}) \equiv f(z|\mathbf{x})$ , where  $\mathbf{x}$  here represents our photomet-  
 518 ric covariates and errors. **FlexZBoost** expands the unknown

10 <https://github.com/ixkael/Delight>

11 <https://github.com/tpospisi/flexcode>;  
<https://github.com/rizbicki/FlexCoDE>

519 function  $f(z|\mathbf{x}) = \sum_i \beta_i(\mathbf{x})\phi_i(z)$  using an orthonormal ba-  
 520 sis  $\{\phi_i(z)\}_i$ . By the orthogonality property, the expansion  
 521 coefficients  $\beta_i(\mathbf{x}) = \mathbb{E}[\phi_i(z)|\mathbf{x}] \equiv \int f(z|\mathbf{x})\phi_i(z)dz$  are thus  
 522 conditional means. The expectation value  $\mathbb{E}[\phi_i(z)|\mathbf{x}]$  of the  
 523 expansion coefficients conditioned on the data is equivalent  
 524 to the regression of the space of possible redshifts on the  
 525 space of possible photometry. Thus the expansion coeffi-  
 526 cients  $\beta_i(\mathbf{x})$  can be estimated from the data via regression  
 527 to yield the conditional density estimate  $\hat{f}(z|\mathbf{x})$ .

528 In this paper, we used `xgboost` (Chen & Guestrin  
 529 2016) for the regression; it should however be noted that  
 530 `FlexCode-RF`<sup>11</sup>, based on Random Forests, generally per-  
 531 forms better for smaller datasets. As our basis  $\phi_i(z)$ , we  
 532 choose a standard Fourier basis. The two tuning parame-  
 533 ters in our photo- $z$  PDF estimate are the number  $I$  of terms  
 534 in the series expansion and an exponent  $\alpha$  that we use to  
 535 sharpen the computed density estimates  $\tilde{f}(z|\mathbf{x}) \propto \hat{f}(z|\mathbf{x})^\alpha$ .  
 536 Both  $I$  and  $\alpha$  were chosen in an automated way by mini-  
 537 mizing the weighted  $L_2$ -loss function (Eq. 5 in Izbicki & Lee  
 538 2017) on a validation set comprised of a randomly selected  
 539 15% of the DC1 training set. While `FlexCode`'s lossless na-  
 540 tive encoding stores each photo- $z$  PDF using the basis co-  
 541 efficients  $\beta_i(\mathbf{x})$ , we discretized the final estimates into 200  
 542 linearly-spaced redshift bins  $0 < z < 2$  to match the consis-  
 543 tent output format of the experimental conditions.

### 544 3.2.5 GP $_z$

545 GP $_z$ <sup>12</sup> (Almosallam et al. 2016a,b) is a sparse Gaussian pro-  
 546 cess based code, a scalable approximation of full Gaus-  
 547 sian Processes (Rasmussen & Williams 2006), that pro-  
 548 duces input-dependent variance estimates corresponding to  
 549 heteroscedastic noise. The model assumes a Gaussian pos-  
 550 terior probability  $p(z|\mathbf{x}) = \mathcal{N}(z|\mu(\mathbf{x}), \sigma(\mathbf{x})^2)$  of the out-  
 551 put redshift  $z$  given the input photometry  $\mathbf{x}$ . The mean  
 552  $\mu(\mathbf{x})$  and the variance  $\sigma(\mathbf{x})^2$  are modeled as functions  
 553  $f(\mathbf{x}) = \sum_{i=1}^m w_i \phi_i(\mathbf{x})$  linear combinations of  $m$  basis func-  
 554 tions  $\{\phi_i(\mathbf{x})\}_{i=1}^m$  with associated weights  $\{w_i\}_{i=1}^m$ . The de-  
 555 tails on how to learn the parameters of the model and the  
 556 hyper-parameters of the basis functions are described in Al-  
 557 mosallam et al. (2016b). GP $_z$ 's variance estimate is composed  
 558 of a model uncertainty term corresponding to sparsity of the  
 559 training set photometry and a noise uncertainty term en-  
 560 compassing noisy photometric observations, enabling quan-  
 561 tification of any need for more representative or more precise  
 562 training samples. GP $_z$  may also weight training set samples  
 563 by importance according to  $|z_{\text{spec}} - z_{\text{phot}}|/(1+z_{\text{spec}})$  to min-  
 564 imize the normalized photo- $z$  point estimate error, however,  
 565 this function may be adapted to photo- $z$  PDFs, pressuring  
 566 the model to dedicate more resources to test set galaxies  
 567 that are not well-represented in the training set.

568 To smooth the long tail in the distribution of magni-  
 569 tude errors, we use the log of the magnitude errors, im-  
 570 proving numerical stability and eliminating the need for  
 571 constraints on the optimization process. Unobserved mag-  
 572 nitudes  $x_u = \mu_u + \Sigma_{uo}\Sigma_{oo}^{-1}(x_o - \mu_o)$  were imputed from  
 573 observed magnitudes  $x_o$  and the training set mean  $\mu$  and  
 574 covariance  $\Sigma$  using a linear model. This is the optimal ex-  
 575 pected value of the unobserved variables given the observed

576 ones under the assumption that the distribution is jointly  
 577 Gaussian; note that this reduces to a simple average if the  
 578 covariates are independent with  $\Sigma_{uo} = 0$ . We reserved for  
 579 validation 20% of the training set and used the Variable  
 580 Covariance option in GP $_z$  with 200 basis functions (see Al-  
 581 mosallam et al. (2016b) for details), neglecting to apply cost-  
 582 sensitive learning options.

### 583 3.2.6 METAPhōR

584 Machine-learning Estimation Tool for Accurate Photomet-  
 585 ric Redshifts (METAPhōR<sup>13</sup>, Cavuoti et al. 2017) is based on  
 586 the Multi Layer Perceptron with Quasi Newton Algorithm  
 587 (MLPQNA) with the least square error model and Tikhonov  
 588  $L_2$ -norm regularization (Hofmann & Mathé 2018). Photo- $z$   
 589 PDFs are generated by running  $N$  trainings on the same  
 590 training set, or  $M$  trainings on  $M$  different random sam-  
 591 plings of the training set. Upon regression of the test set,  
 592 the photometry  $m_{ij}$  of each test set galaxy  $j$  in filter  $i$  is  
 593 perturbed according to  $m'_{ij} = m_{ij} + \alpha_i F_{ij} \epsilon$  in terms of  
 594 the standard normal random variable  $\epsilon \sim \mathcal{N}(0, 1)$ , a mul-  
 595 tiplicative constant  $\alpha_i$  permitting accommodation of multi-  
 596 survey photometry, and a bimodal function  $F_{ij}$  composed of  
 597 a polynomial fit of the mean magnitude errors on the binned  
 598 bands plus a constant term representing the threshold be-  
 599 low which the polynomial's noise contribution is negligible  
 600 (Brescia et al. 2018).

601 In this work, we used a hierarchical KNN to replace  
 602 non-detections with values based on their neighbors. The  
 603 usual cross-validation of redshift estimates and PDFs was  
 604 also omitted for this study.

### 605 3.2.7 SkyNet

606 SkyNet<sup>14</sup> (Graff et al. 2014) employs a neural network based  
 607 on a second order conjugate gradient optimization scheme  
 608 (see Graff et al. 2014, for further details). The neural net-  
 609 work is configured as a standard multilayer perceptron with  
 610 three hidden layers and one input layer with 12 nodes cor-  
 611 responding to the 6 photometric magnitudes and their mea-  
 612 surement errors.

613 SkyNet's classifier mode uses a cross-entropy error func-  
 614 tion with a 20:40:40 node (all rectified linear units) architec-  
 615 ture for each hidden layer and an output layer of 200 nodes  
 616 corresponding to 200 bins for the PDF, with a softmax acti-  
 617 vation function to enforce the normalization condition that  
 618 the probabilities sum to unity. While previous implemen-  
 619 tations of the code (see Appendix C.3 of Sánchez et al. 2014;  
 620 Bonnett 2015) implement a sliding bin smoothing, no such  
 621 procedure was used in this study.

622 We pre-whitened the data by pegging the magnitudes  
 623 to (45,45,40,35,42,42) and errors to (20,20,10,5,15,15) for  
 624 *ugrizy* filters, respectively. To avoid over-fitting, 30% of the  
 625 training set was reserved for validation, and training was  
 626 halted as soon as the error rate began to increase on the  
 627 validation set. The weights were randomly initialized based  
 628 on normal sampling.

<sup>12</sup> <https://github.com/OxfordML/GPz>

<sup>13</sup> <http://dame.dsfa.unina.it>

<sup>14</sup> <http://ccforge.cse.rl.ac.uk/gf/project/skynet/>

## 8 LSST Dark Energy Science Collaboration

### 3.2.8 TPZ

Trees for Photo- $z$ (TPZ<sup>15</sup>, Carrasco Kind & Brunner 2013; Carrasco Kind & Brunner 2014) uses prediction trees and random forest techniques to estimate photo- $z$  PDFs. TPZ recursively splits the training set into branch pairs based on maximizing information gain among a random subsample of features, to minimize correlation between the trees, terminating only when a newly created leaf meets a criterion, such as a leaf size minimum or a variance threshold. The regions in each terminal leaf node correspond to a subsample of the training set with similar properties. Bootstrap samples from the training set photometry and errors are used to build a set of prediction trees.

To run TPZ, we replaced non-detections with an approximation of the  $1\sigma$  detection threshold based on the error forecast of the 10-year LSST data, i. e.  $dm = 2.5 \log(1 + N/S)$  where  $dm \sim 0.7526$  magnitudes for  $N/S = 1$ . We calibrated TPZ with the Out-of-Bag cross-validation technique (Breiman et al. 1984; Carrasco Kind & Brunner 2013) to evaluate its predictive validity and determine the relative importance of the different input attributes. We grew 100 trees to a minimum leaf size of 5 using the *ugri* magnitudes, all  $u - g, g - r, r - i, i - z, z - y$  colours, and the associated errors, as the  $z$  and  $y$  magnitudes did not show significant correlation with the redshift in our cross-validation. We partitioned our redshift space into 200 bins and smoothed each individual PDF with a smoothing scale of twice the bin size.

### 3.3 trainZ: a pathological photo- $z$ PDF estimator

We also consider a pathological photo- $z$  PDF estimation method, dubbed **trainZ**, which assigns each test set galaxy a photo- $z$  PDF equal to the normalized redshift distribution  $N(z)$  of the training set, according to

$$p(z|\{z_j\}) \equiv \frac{1}{N_{\text{train}}} \sum_{i=1}^{N_{\text{train}}} \begin{cases} 1 & \text{if } z_k \leq z_i < z_{k+1} \\ 0 & \text{otherwise} \end{cases}. \quad (2)$$

Unlike the other methods, the **trainZ** estimator is *independent of the photometric data*, effectively performing a KNN procedure with  $k = N_{\text{train}}$ .

Though **trainZ** is strongly vulnerable to a nonrepresentative training set, it should optimize performance metrics probing the ensemble properties of the galaxy sample, modulo Poisson error due to small sample size, as the training set and test set are drawn from the same underlying population. We will demonstrate its performance under the metrics of Section 4 and discuss it as an illustrative experimental control case in Section 6.1 to highlight the limitations of our evaluation criteria for photo- $z$  PDFs.

## 4 ANALYSIS

The goal of this study is to evaluate the degree to which photo- $z$  PDFs of each method can be trusted for a generic analysis. The overloaded “ $p(z)$ ” is a widespread abuse of notation that obfuscates this goal, so we dedicate attention

to dismantling it here. Galaxies have redshifts  $z$  and photometric data  $d$  drawn from a joint probability space  $p(z, d)$  in nature. As a result, each observed galaxy  $i$  has a *true posterior photo- $z$  PDF*  $p(z|d_i)$  as well as a true likelihood  $p(d|z_i)$ . There are a number of metrics that can be used to test the accuracy of a photo- $z$  posterior as an estimator of a true photo- $z$  posterior if the true photo- $z$  PDF is known. However, the true photo- $z$  PDF is in general not accessible unless the photometry is in fact drawn from a ground truth for the joint probability density of redshift and photometry  $p(z, d)$ . In contrast, existing mock catalogs produce redshift-photometry pairs  $(z, d)$  by a deterministic algorithm that does not correspond to a joint probability density from which one can take samples. In these cases there is no “true PDF” for an individual object, and most measures of PDF fidelity will necessarily be restricted to probing the quality of the ensemble of photo- $z$  PDFs. (See §6.2 for a discussion of how one might circumvent this limitation.)

Before describing the metrics appropriate to the DC1 data set, we outline the philosophy behind our choices. A photo- $z$  PDF estimator derived by method  $H$  must be understood as a posterior probability distribution

$$\hat{p}_i^H(z) \equiv p(z|d_i, I_D, I_H), \quad (3)$$

conditioned not only on the photometric data  $d_i$  for that galaxy but also on parameters encompassing a number of things that will differ depending on the method  $H$  used to produce it, namely the often implicit assumptions  $I_H$  necessary for the method to be valid and any inputs  $I_D$  it takes as prior information, such as a template library or training set. Because of this, direct comparison of photo- $z$  PDFs produced by different methods is in some sense impossible; even if they share the same external prior information  $I_D$ , by definition they cannot be conditioned on the same assumptions  $I_H$ , otherwise they would not be distinct methods at all. We call  $I_H$  the *implicit prior* specific to the method, though some aspects of its nature may be discerned.

In this study, we isolate the effect of differences in prior information  $I_H$  specific to each method by using a single training set  $I_D^{\text{ML}}$  for all machine learning-based codes and a single template library  $I_D^T$  for all template-based codes. These sets of prior information are carefully constructed to be representative and complete, so we have  $I_D \equiv I_D^{\text{ML}} \equiv I_D^T$  for every method  $H$ . Under this assumption, a ratio of posteriors of codes is in effect a ratio of the implicit posteriors  $p(z|d_i, I_H')$  since the external prior information  $I_D$  is present in the numerator and denominator. Thus comparisons of  $\hat{p}_i^H(z)$  isolate the effect of the method used to obtain the estimator, which should enable interpretation of the differences between estimated PDFs in terms of the specifics of the method implementations.

The exact implementation of the metrics theoretically depends on the parametrization of the photo- $z$  PDFs, which may differ across codes and can affect the precision of the estimator (Malz et al. 2018). Even considering a single method under the same parametrization, such as the 200-bin  $0 < z < 2$  piecewise constant function used here, the exact bin definitions will affect the result. The piecewise constant format is chosen because of its established presence in the literature, and the choice of 200 bins was motivated by the approximate number of columns expected to be available for

<sup>15</sup> <https://github.com/mgckind/MLZ>

storage of photo- $z$  PDFs for the final LSST Project tables.<sup>16</sup> We will discuss the choice of photo- $z$  PDF parameterization further in Section 6.

This analysis is conducted using the `qp`<sup>17</sup> software package (Malz & Marshall 2018) for manipulating and calculating metrics of univariate PDFs. We present the metrics of photo- $z$  PDFs that address our goals in the sections below. Section 4.1 outlines aggregate metrics of a catalogue of photo- $z$  PDFs, and Section 4.2 presents a metric of individual photo- $z$  PDFs in the absence of true photo- $z$  PDFs. Though the outmoded practices should not be encouraged, those seeking a connection to previous comparison studies will find metrics of redshift point estimate reductions of photo- $z$  PDFs in Appendix B and metrics of a science-specific summary statistics heuristically derived from photo- $z$  PDFs in Appendix A.

#### 4.1 Metrics of photo- $z$ PDF ensembles

Because LSST’s photo- $z$  PDFs will be used for many scientific applications, some of which require accuracy of each individual catalog entry, we consider several metrics that probe the population-level performance of the photo- $z$  PDFs. Because we have the true redshifts but not true photo- $z$  PDFs for comparison, we remind the reader of the Cumulative Distribution Function (CDF)

$$\text{CDF}[f, q] \equiv \int_{-\infty}^q f(z) dz, \quad (4)$$

of a generic univariate PDF  $f(z)$ , which is used as the basis for several of our metrics.

A quantile of a distribution is the value  $q$  at which the CDF of the distribution is equal to  $Q$ ; percentiles and quartiles are familiar examples of linearly spaced sets of 100 and 4 quantiles, respectively. The quantile-quantile (QQ) plot serves as a graphical visualization for comparing two distributions, where the quantiles of one distribution are plotted against the quantiles of the other distribution, providing an intuitive way to qualitatively assess the consistency between an estimated distribution and a true distribution. The closer the QQ plot is to diagonal, the closer the match between the distributions.

The probability integral transform (PIT)

$$\text{PIT} \equiv \text{CDF}[\hat{p}, z_{\text{true}}] \quad (5)$$

is the CDF of a photo- $z$  PDF evaluated at its true redshift, and the distribution of PIT values probes the average accuracy of the photo- $z$  PDFs of an ensemble of galaxies. The distribution of PIT values is effectively the derivative of the QQ plot. A catalogue of accurate photo- $z$  PDFs should have a PIT distribution that is uniform  $U(0, 1)$ , and deviations from flatness are interpretable: overly broad photo- $z$  PDFs induce underrepresentation of the lowest and highest PIT values, whereas overly narrow photo- $z$  PDFs induce overrepresentation of the lowest and highest PIT values. Catastrophic outliers with a true redshift outside the support of its photo- $z$  PDF have  $\text{PIT} \approx 0$  or  $\text{PIT} \approx 1$ .

<sup>16</sup> See, e. g. the LSST Data Products Definition Document, available at: <https://ls.st/dpdd>

<sup>17</sup> <http://github.com/aimalz/qp/>

The PIT distribution has been used to quantify the performance of photo- $z$  PDF methods in the past (e. g. Bordoloi et al. 2010; Polsterer et al. 2016; Tanaka et al. 2018). Tanaka et al. (2018) use the histogram of PIT values as a diagnostic indicator of overall code performance, while Freeman et al. (2017) independently define the PIT and demonstrate how its individual values may be used both to perform hypothesis testing (via, e. g. the KS, CvM, and AD tests; see below) and to construct quantile-quantile plots. Following Kodra & Newman (in prep.) we define the PIT-based catastrophic outlier rate as the fraction of galaxies with  $\text{PIT} < 0.0001$  or  $\text{PIT} > 0.9999$ , which should total 0.0002 for an ideal uniform distribution.

We evaluate a number of quantitative metrics derived from the visually interpretable QQ plot and PIT histogram, built on the Kolmogorov-Smirnov (KS) statistic

$$\text{KS} \equiv \max_z \left( \left| \text{CDF}[\hat{f}, z] - \text{CDF}[\tilde{f}, z] \right| \right), \quad (6)$$

interpretable as the maximum difference between the CDFs of an approximating univariate distribution  $\hat{f}(z)$  and a reference distribution  $\tilde{f}(z)$ , in this case  $U(0, 1)$ . We also consider two variants of the KS statistic. A cousin of the KS statistic, the Cramer-von Mises (CvM) statistic

$$\text{CvM}^2 \equiv \int_{-\infty}^{+\infty} (\text{CDF}[\hat{f}, z] - \text{CDF}[\tilde{f}, z])^2 d\text{CDF}[\tilde{f}, z] \quad (7)$$

is the mean-squared difference between the CDFs of an approximate and true PDF. The Anderson-Darling (AD) statistic

$$\text{AD}^2 \equiv N_{\text{tot}} \int_{-\infty}^{+\infty} \frac{(\text{CDF}[\hat{f}, z] - \text{CDF}[\tilde{f}, z])^2}{\text{CDF}[\tilde{f}, z](1 - \text{CDF}[\tilde{f}, z])} d\text{CDF}[\tilde{f}, z] \quad (8)$$

is a weighted mean-squared difference featuring enhanced sensitivity to discrepancies in the tails of the distribution. In anticipation of a substantial fraction of galaxies having PIT of 0 or 1, a consequence of catastrophic outliers, we evaluate the AD statistic with modified bounds of integration (0.01, 0.99) to exclude those extremes in the name of numerical stability.

#### 4.2 Conditional Density Estimate (CDE) Loss: a metric of individual photo- $z$ PDFs

The BUZZARD simulation process precludes testing the degree to which samples from our photo- $z$  posteriors reconstruct the space of  $p(z, \text{data})$ . To the knowledge of the authors, there is only one metric that can be used to evaluate the performance of individual photo- $z$  PDF estimators in the absence of true photo- $z$  posteriors. Using the notation introduced in Section 3.2.4, the conditional density estimation (CDE) loss is defined as

$$L(f, \hat{f}) \equiv \int \int (f(z|\mathbf{x}) - \hat{f}(z|\mathbf{x}))^2 dz dP(\mathbf{x}) \quad (9)$$

in terms of the photometry  $\mathbf{x}$ , an analogue to the familiar root-mean-square-error used in conventional regression. We estimate the CDE loss via

$$\hat{L}(f, \hat{f}) = \mathbb{E}_{\mathbf{x}} \left[ \int \hat{f}(z | \mathbf{X})^2 dz \right] - 2\mathbb{E}_{\mathbf{x}, Z} \left[ \hat{f}(Z | \mathbf{X}) \right] + K_f, \quad (10)$$

where the first term is the expectation value of the photo- $z$  posterior with respect to the marginal distribution of the photometric covariates  $\mathbf{X}$ , the second term is the expectation value with respect to the joint distribution of  $\mathbf{X}$  and the space  $Z$  of all possible redshifts, and the third term  $K_f$  is a constant depending only upon the true conditional densities  $f(z|\mathbf{x})$ . We may estimate these expectations empirically on the test or validation data (Eq. 7 in Izbicki et al. 2017) without knowledge of the true densities.

## 5 RESULTS

We begin with a demonstrative visual inspection of the photo- $z$  PDFs produced by each code for individual galaxies. Figure 1 shows the photo- $z$  PDFs for four galaxies chosen as examples of photo- $z$  PDF archetypes: a narrow unimodal PDF, a broad unimodal PDF, a bimodal PDF, and a multimodal PDF. We reiterate that under our idealized experimental conditions, differences between codes are the isolated signature of the implicit prior due to the method by which the photo- $z$  PDFs were derived.

The most striking differences between codes are the small-scale features induced by the interaction between the shared piecewise constant parameterization of 200 bins  $0 < z < 2$  of Section 4 and the smoothing conditions or lack thereof in each algorithm. The  $dz = 0.01$  redshift resolution is sufficient to capture the broad peaks of faint galaxies’ photo- $z$  PDFs with large photometric errors but is too broad to resolve the narrow peaks for bright galaxies’ photo- $z$  PDFs with small photometric errors. This observation is consistent with the findings of Malz et al. (2018) that the piecewise constant parameterization underperforms in the presence of small-scale structures.

However, the shared small-scale features of ANNz2, METAPhoR, CMNN, and SkyNet are a result of various weighted sums of the limited number of training set galaxies with colors similar to those of the test set galaxy in question, with behavior closer to classification than regression in the case of ANNz2. The settings used on GPz in this work forced broadening of the single Gaussian to cover the multimodal redshift solutions of the other codes.

### 5.1 Performance on photo- $z$ PDF ensembles

The histogram of PIT values, QQ plot, and QQ difference plot relative to the ideal diagonal are provided in Figure 2, showcasing the biases and trends in the average accuracy of the photo- $z$  PDFs for each code. The high QQ values (i. e. more high than low PIT values) of BPZ, CMNN, Delight, EAZY, and GPz indicate photo- $z$  PDFs biased low, and the low QQ values (more low than high PIT values) of SkyNet and TPZ indicate photo- $z$  PDFs biased high. The gray shaded band marks the  $2\sigma$  variance in PIT values found using the trainZ algorithm with a bootstrap resampling of the training set and a sample size of 30,000 galaxies, representing a very conservative estimate of the representative training sample size, and thus an approximate minimal error significance compared to ideal performance. Deviations in the PIT histograms outside of this range show that significant biases are present for some codes.

The PIT histograms of Delight, CMNN, SkyNet, and TPZ

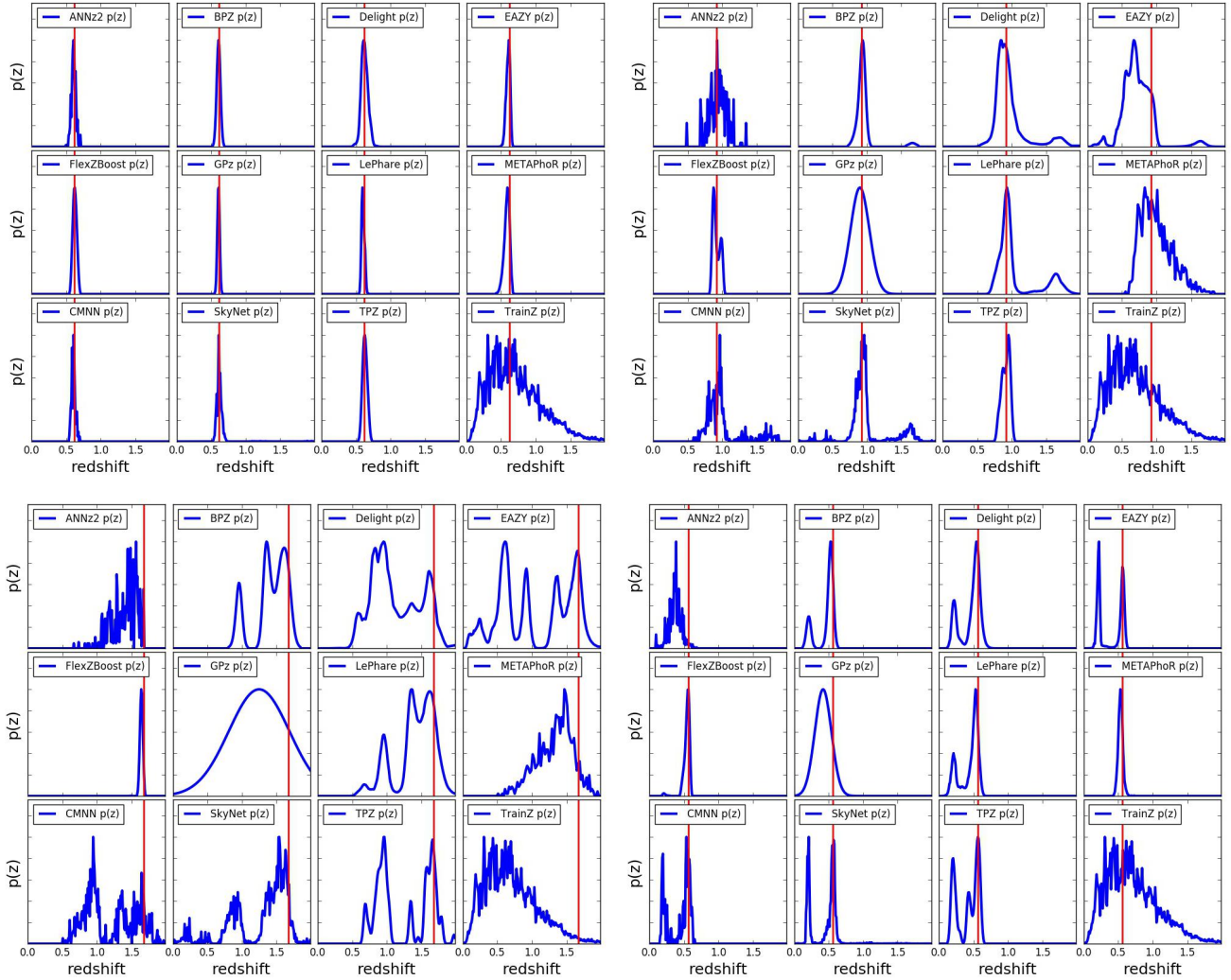
**Table 2.** The catastrophic outlier rate as defined by extreme PIT values. We expect a value of 0.0002 for a proper Uniform distribution. An excess over this small value indicates true redshifts that fall outside the non-zero support of the  $p(z)$ .

Photo- $z$ Code	fraction PIT < $10^{-4}$ or > 0.999
ANNz2	0.0265
BPZ	0.0192
Delight	0.0006
EAZY	0.0154
FlexZBoost	0.0202
GPz	0.0058
LePhare	0.0486
METAPhoR	0.0229
CMNN	0.0034
SkyNet	0.0001
TPZ	0.0130
trainZ	0.0002

feature an underrepresentation of extreme values, indicative of overly broad photo- $z$  PDFs, while the overrepresentation of extreme values for METAPhoR indicate overly narrow photo- $z$  PDFs. These five codes in particular have a free parameter for bandwidth, which may be responsible for this vulnerability, in spite of the opportunity for fine-tuning with perfect prior information. FlexZBoost’s “sharpening” parameter (described in Section 3.2.4) played a key role in diagonalizing the QQ plot, indicating a common avenue for improvement in the approaches that share this type of parameter. On the other hand, the three purely template-based codes, BPZ, EAZY, and LePhare, do not exhibit much systematic broadening or narrowing, which may indicate that complete template coverage effectively defends from these effects.

Close inspection of the extremes at PIT values of 0 and 1 reveal spikes in the first and last bin of the PIT histogram for some codes in Figure 2, corresponding to catastrophic outliers where the true redshift lies outside of the support of the  $p(z)$ . The catastrophic outlier rates are provided in Table 2. As expected, trainZ achieves precisely the 0.0002 value expected of an ideal PIT distribution. ANNz2, FlexZBoost, LePhare, and METAPhoR have notably high catastrophic outlier rates  $> 0.02$ , exceeding 100 times the ideal PIT rate, meriting further investigation.

Figure 3 highlights the relative values of the KS, CvM, and AD test statistics calculated by comparing the PIT distribution and a uniform distribution  $U(0, 1)$ . METAPhoR and LePhare perform well under the AD but poorly under the KS and CvM due to their high catastrophic outlier rates. ANNz2 and FlexZBoost are the top scorers under these metrics of the PIT distribution. ANNz2’s strong performance can be attributed to an aspect of the training process in which training set galaxies with a PIT that more closely matches the percentiles of the DC1 training set’s redshift distribution are upweighted; in effect, these quantile-based metrics were part of the algorithm itself that may or may not serve it well under more realistic experimental conditions. Similar to what was done for the PIT histograms in Figure 2, we create bootstrap training samples of 30,000 galaxies for use with trainZ in order to estimate a conservative statistical floor that we would expect in real data. No code reaches this idealized floor, indicating that all codes suffer some degra-



**Figure 1.** The individual photo- $z$  PDFs (blue) distributions produced by the twelve codes (small panels) on four exemplary galaxies' photometry (large panels) with different true redshifts (red). The photo- $z$  PDFs of all codes share some features for the example galaxies due to physical color degeneracies and photometric errors: tight unimodal  $p(z)$  (upper left), broad unimodal  $p(z)$  (upper right), bimodal  $p(z)$  (lower right), and complex/multimodal  $p(z)$  (lower left). The diverse algorithms and implementations induce differences in small-scale structure and sensitivity to physical systematics.

940 dation from the ideal when employing their implicit priors,  
 941 though ANNz2, FlexZBoost, and GPz are within a factor of  
 942 two.

## 943 5.2 Performance on individual photo- $z$ PDFs

944 The values of the CDE loss statistic of individual photo- $z$   
 945 PDF accuracy are provided in Table 3. It is worth noting  
 946 that strong performance on the CDE loss, corresponding to  
 947 lower values of the metric, should imply strong performance  
 948 on the other metrics, though the inverse is not necessarily  
 949 true. Thus the CDE loss is the most effective metric for  
 950 generic science cases.

951 Of the metrics we were able to consider in this experiment,  
 952 the **CDE Loss** is the only metric that can ap-  
 953 propriately penalize the pathological trainZ. Addi-  
 954 tionally, it favors CMNN and FlexZBoost, the latter of which is  
 955 optimized for this metric.

**Table 3.** CDE loss statistic of the individual photo- $z$  PDFs for each code. A lower value of the CDE loss indicates more accurate individual photo- $z$  PDFs, with CMNN and FlexZBoost performing best under this metric.

Photo- $z$ Code	CDE Loss
ANNz2	-6.88
BPZ	-7.82
Delight	-8.33
EAZY	-7.07
FlexZBoost	-10.60
GPz	-9.93
LePhare	-1.66
METAPhR	-6.28
CMNN	-10.43
SkyNet	-7.89
TPZ	-9.55
trainZ	-0.83

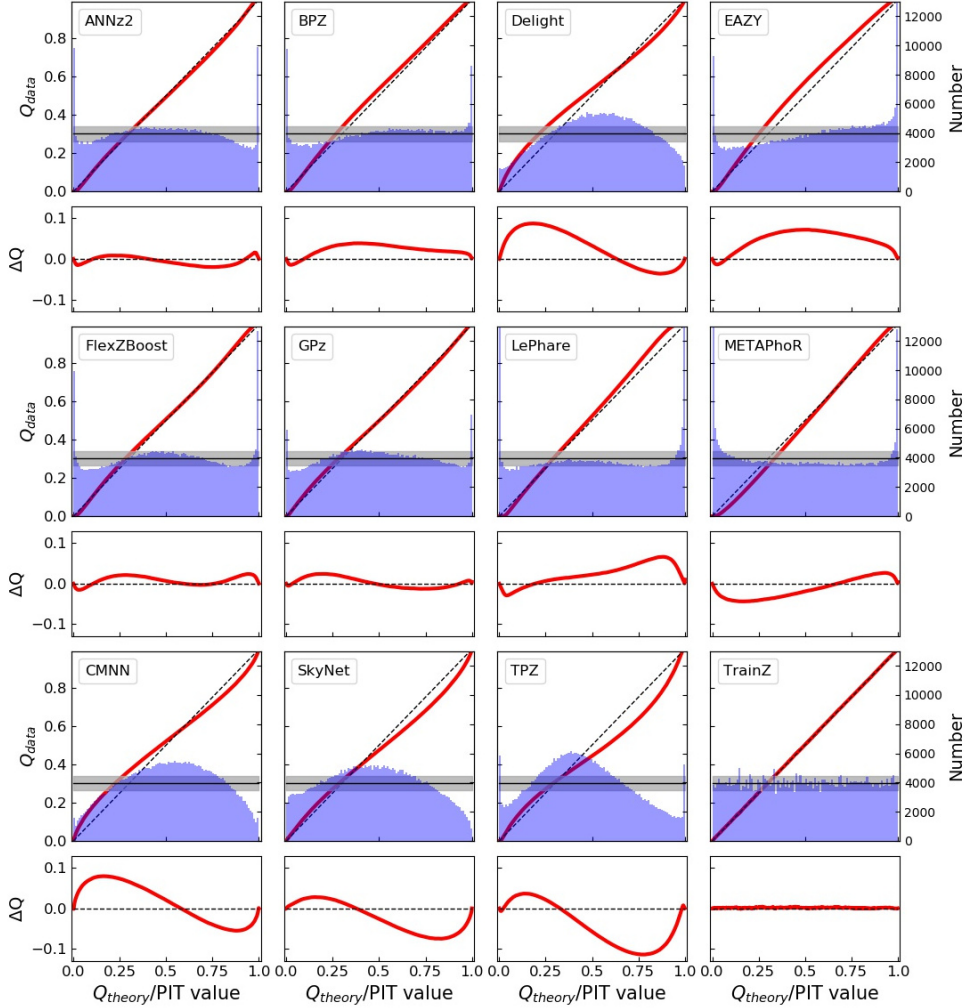


**Figure 2.** The QQ plot (red) and PIT histogram (blue) of the photo- $z$  PDF codes (panels) along with the ideal QQ (black dashed diagonal) and ideal PIT (gray horizontal) curves, as well as a difference plot for the QQ difference from the ideal diagonal (lower inset). The gray shaded region indicates the  $2\sigma$  range from a bootstrap resampling of the training set with a size of 30,000 galaxies using `trainZ`. The twelve codes exhibit varying degrees of four deviations from perfection: an overabundance of PIT values at the centre of the distribution indicate a catalogue of overly broad photo- $z$  PDFs, an excess of PIT values at the extrema indicates a catalogue of overly narrow photo- $z$  PDFs, catastrophic outliers manifest as overabundances at PIT values of 0 and 1, and asymmetry indicates systematic bias, a form of model misspecification. Values in excess of the  $2\sigma$  shaded region show that for some codes these errors will be significant given expected training sample sizes.

## 956 6 DISCUSSION AND FUTURE WORK

957 In contrast with other photo- $z$  PDF comparison papers that  
 958 have aimed to identify the “best” code for a given survey, we  
 959 have focused on the somewhat more philosophical questions  
 960 of how to assess photo- $z$  PDF methods and how to interpret  
 961 differences between codes in terms of photo- $z$  PDF per-  
 962 formance. In Section 6.1, we reframe the strong performance of  
 963 our pathological photo- $z$  PDF technique, `trainZ`, as a cau-  
 964 tionary tale about the importance of choosing appropriate  
 965 comparison metrics. In Section 6.2, we outline the experi-  
 966 ments we intend to build upon this study. In Section 6.3, we  
 967 discuss the enhancements of the mock data set that will be  
 968 necessary to enable the future experiments.

### 969 6.1 Interpretation of metrics

970 We remind the reader that contributed codes were given a  
 971 goal of obtaining accurate photo- $z$  PDFs, not an accurate  
 972 stacked estimator of the redshift distribution, so we do not  
 973 expect the same codes to necessarily perform well for both  
 974 classes of metrics. Indeed, the codes were optimized for their  
 975 interpretation of our request for “accurate photo- $z$  PDFs,”  
 976 and we expect that the implementations would have been  
 977 adjusted had we requested optimization of the traditional  
 978 metrics of Appendices A and B.

979 Furthermore, our metrics are not necessarily able to as-  
 980 sess the fidelity of individual photo- $z$  PDFs relative to true  
 981 posteriors: in the absence of a “true PDF” from which red-  
 982 shifts are drawn, it is difficult to construct metrics to mea-  
 983 sure performance for individual galaxies rather than ensem-

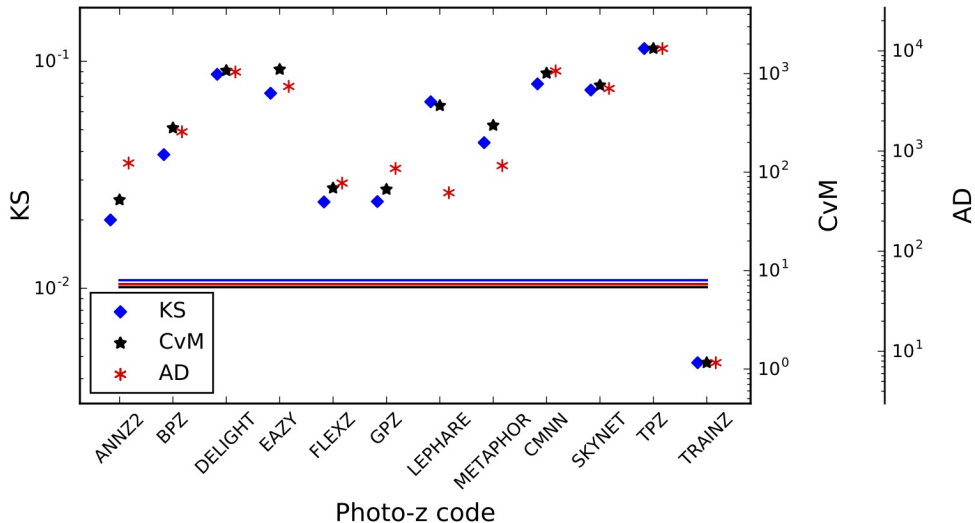


**Figure 3.** A visualization of the Kolmogorov-Smirnov (KS, blue diamond), Cramer-von Mises (CvM, black star), and Anderson-Darling (AD, red asterisk) statistics for the PIT distributions. There is generally good agreement between these statistics, with differences corresponding to the codes with outstanding catastrophic outlier rates, a reflection in the differences in how each statistic weights the tails of the distribution. Horizontal lines indicate the level of uncertainty found by bootstrapping a training set sample of 30,000 galaxies using `trainZ`; none of the codes reach this conservative ideal floor in expected uncertainty.

bles. (The CDE Loss metric of section 4.2 is an exception to this rule.) A lack of appropriate metrics more sophisticated than the CDE Loss remains an open issue for science cases requiring accurate individual galaxy PDFs. The metric-specific performance demonstrated in this paper implies that we may need multiple photo- $z$  PDF approaches tuned to each metric in order to maximize returns over all science cases in large upcoming surveys.

The `trainZ` estimator of Section 3.3, which assigns every galaxy a photo- $z$  PDF equal to  $N(z)$  of the training set, is introduced as an experimental control or null test to demonstrate this point via *reductio ad absurdum*. Because our training set is perfectly representative of the test set,  $N(z)$  should be identical for both sets down to statistical noise. **We make the alarming observation that `trainZ`, the experimental control, outperforms all codes on the CDF-based metrics, and all but one code on the  $N(z)$  based statistics.** The PIT and other CDF-based metrics upon which modern photo- $z$  PDF comparisons are built can be gamed by a trivial estimator that yields only an affirmation of prior knowledge uninformed by the data. In other words, such ensemble metrics are not appropriate for the task of selecting photo- $z$  PDF codes for analysis pipelines.

The CDE loss and point estimate metrics appropriately penalize `trainZ`'s naivete. As shown in Appendix B, `trainZ` has identical `ZPEAK` and `ZWEIGHT` values for every galaxy, and thus the photo- $z$  point estimates are constant as a function of true redshift, i. e. a horizontal line at the mode and mean of the training set distribution respectively. The explicit dependence on the individual posteriors in the calculation of the CDE loss, described in Section 5.2, distinguishes this metric from those of the photo- $z$  PDF ensemble and stacked estimator of the redshift distribution, despite their prevalence in the photo- $z$  literature.

In summary, context is crucial to defend against deceptively strong performers such as `trainZ`; the best photo-

**$z$  PDF method is the one that most effectively achieves our science goals**, not the one that performs best on a metric that does not reflect those goals. In the absence of a single scientific motivation or the information necessary for a principled metric definition, we must consider many metrics and be critical of the information transmitted by each.

## 6.2 Extensions to the experimental design

The work presented in this paper is only a first step in assessing photo- $z$  PDF approaches and moving toward an improved photometric redshift estimator. Here we discuss the next steps for subsequent investigations.

This initial paper explores photo- $z$  PDF code performance in idealized conditions with perfect catalog-based photometry and representative training data, but the resilience of each code to such realistic imperfections in prior information has not yet been evaluated. A top priority for a follow-up study is to test realistic forms of incomplete, erroneous, and non-representative template libraries and training sets as well as the impact of other forms of external priors that must be ingested by the codes, major concerns in Newman et al. (2015); Masters et al. (2017). Outright redshift failures due to emission line misidentification or noise spikes may be modeled by the inclusion of a small number of high-confidence yet false redshifts. We plan to perform a full sensitivity analysis on a realistically incomplete training set of spectroscopic galaxies, modeling the performance of spectrographs, emission-line properties, and expected signal-to-noise to determine which potential training set galaxies are most likely to be excluded.

Appendix A only addresses the stacked estimator of the redshift distribution of the entire galaxy catalogue rather than subsets in bins, tomographic or otherwise. The effects of tomographic binning scheme will be explored in a dedi-

cated future paper, including propagation of redshift uncertainties in a set of fiducial tomographic redshift bins in order to estimate impact on cosmological parameter estimation.

Sequels to this study will also address some shortcomings of our experimental procedure. The fixed redshift grid shared between the codes may have unfairly penalized codes with a different native parameterization, as precision is lost when converting between formats. Performance on the (admittedly small) population of sharply peaked photo-z PDFs may have been suppressed across all codes due to the insufficient resolution of the redshift grid. In light of the results of Malz et al. (2018), in future analyses we plan to switch from a fixed grid to the quantile parameterization or to permit each code to use its native storage format under a shared number of parameters.

Section 4 discussed the difficulty in evaluating PDF accuracy for individual objects. In a follow-up study, we will generate “true PDF” distributions, yielding a dataset that enables a test of PDF accuracy for individual galaxies rather than solely ensembles.

### 6.3 Realistic mock data

To make optimal use of the LSST data for cosmological and other astrophysical analyses of the LSST-DESC Science Roadmap, future investigations that build upon this one will require a more sophisticated set of galaxy photometry and redshifts. This initial paper explored a data set that was constructed at the catalog level, with no inclusion of the complications that come from measuring photometry from images. Future data challenges will move to catalogs constructed from mock images, including the complications of deblending, sensor inefficiencies, and heterogeneous observing conditions, all anticipated to affect the measured colours of LSST’s galaxy sample (Dawson et al. 2016).

The DC1 galaxy SEDs were linear combinations of just five basis SED templates, but a next generation of data for photo-z PDF investigations must include a broader range of physical properties. Though we only considered  $z < 2$  here, LSST 10-year data will contain  $z > 2$  galaxies, plagued by fainter apparent magnitudes and anomalous colours due to stellar evolution. A subsequent study must also have a data set that includes low-level active galactic nuclei (AGN) features in the SEDs, which perturb colours and other host galaxy properties. An observational degeneracy between the Lyman break of a  $z \sim 2 - 3$  galaxy from the Balmer break of a  $z \sim 0.2 - 0.3$  galaxy is a known source of catastrophic outliers (Massarotti et al. 2001) that was not effectively included in this study. To gauge the sensitivity of photo-z PDF estimators to catastrophic outliers, our data set must include realistic high-redshift galaxy populations.

The overarching plan describing everything laid out in this section is described in more detail in the LSST-DESC Science Roadmap (see Footnote in Section 1).

## 7 CONCLUSION

This paper compares twelve photo-z PDF codes under controlled experimental conditions of representative and complete prior information to set a baseline for an upcoming

sensitivity analysis. This work isolates the impact on metrics of photo-z PDF accuracy due to the estimation technique as opposed to the complications of realistic physical systematics of the photometry. Though the mock data set of this investigation did not include true photo-z posteriors for comparison, **we interpret deviations from perfect results given perfect prior information as the imprint of the implicit assumptions underlying the estimation approach.**

We evaluate the twelve codes under science-agnostic metrics both established and emerging to stress-test the ensemble properties of photo-z PDF catalogues derived by each method. In appendices, we also present metrics of point estimates and a prevalent summary statistic of photo-z PDF catalogues used in cosmological analyses to enable the reader to relate this work to studies of similar scope. We observe that no one code dominates in all metrics, and that the standard metrics of photo-z PDFs and the stacked estimator of the redshift distribution can be gamed by a very simplistic procedure that asserts the prior over the data. We emphasize to the photo-z community that **metrics used to vet photo-z PDF methods must be scrutinized to ensure they correspond to the quantities that matter to our science.**

## Acknowledgments

Author contributions are listed below.

S.J. Schmidt: Led the project. (conceptualization, data curation, formal analysis, investigation, methodology, project administration, resources, software, supervision, visualization, writing – original draft, writing – review & editing)

A.I. Malz: Contributed to choice of metrics, implementation in code, and writing. (conceptualization, methodology, project administration, resources, software, visualization, writing – original draft, writing – review & editing)

J.Y.H. Soo: Ran ANNz2 and Delight, updated abstract, edited sections 1 through 6, added tables in Methods and Results, updated references.bib and added references throughout the paper

I.A. Almosallam: vetted the early versions of the data set and ran many photo-z codes on it, applied GPz to the final version and wrote the GPz subsection

M. Brescia: main ideator of METAPHOR and of MLPQNA; modification of METAPHOR pipeline to fit the LSST data structure and requirements

S. Cavaudi: Contributed to choice and test of metrics, ran METAPHOR, minor text editing

J. Cohen-Tanugi: contributed to running code, analysis discussion, and editing, reviewing the paper

A.J. Connolly: Developed the colour-matched nearest-neighbours photo-z code; participated in discussions of the analysis.

P.E. Freeman: Contributed to choice of CDE metrics and to implementation of FlexZBoost

M.L. Graham: Ran the colour-matched nearest-neighbours photo-z code on the Buzzard catalog and wrote the relevant piece of Section 2; participated in discussions of the analysis.

K. Iyer: assisted in writing metric functions used to evaluate codes

M.J. Jarvis: Contributed text on AGN to Discussion section

and portions of GPz work  
 J.B. Kalmbach: Worked on preparing the figures for the paper.  
 E. Kovacs: Ran simulations, discussed data format and properties for SEDs, dust, and ELG corrections  
 A.B. Lee: Co-developed FlexZBoost and the CDE loss statistic, wrote text on the work, and supervised the development of FlexZBoost software packages  
 G. Longo: Scientific advise, test and validation of the modified METAPHOR pipeline, text of the METAPHOR section  
 C. B. Morrison: Managerial support; Discussions with authors regarding metrics and style; Some coding contribution to metric computation.  
 J. Newman: Contributions to overall strategy, design of metrics, and supervision of work done by Rongpu Zhou  
 E. Nourbakhsh: Ran and optimized TPZ code and wrote a subsection of Section 2 for TPZ  
 E. Nuss: contributed to running code, analysis discussion, and editing,reviewing the paper  
 T. Pospisil: Co-developed FlexZBoost software and CDE loss calculation code  
 H. Tranin: contributed to providing SkyNet results and writing the relevant section  
 R. Zhou: Optimized and ran EAZY and contributed to the draft  
 R. Izbicki: Co-developed FlexZBoost and the CDE loss statistic, and wrote software for FlexZBoost

by the GridPP Collaboration. This work was performed in part under DOE Contract DE-AC02-76SF00515.

## APPENDIX A: EVALUATION OF THE REDSHIFT DISTRIBUTION

Perhaps the most popular application of photo- $z$  PDFs is the estimation of the overall redshift distribution  $N(z)$ , a quantity that enters some cosmological calculations and the true value of which is known for the DC1 data set and will be denoted as  $\tilde{N}(z)$ . In terms of the prior information provided to each method, the true redshift distribution satisfies the tautology  $\tilde{N}(z) = p(z|I_D)$  due to our experimental set-up; because the DC1 training and template sets are representative and complete,  $I_D$  represents a prior that is also equal to the truth. In this ideal case of complete and representative prior information, the method that would give the best approximation to  $\tilde{N}(z)$  would be one that neglects all the information contained in the photometry  $\{d_i\}_{N_{tot}}$  and gives every galaxy the same photo- $z$  PDF  $\hat{p}_i(z) = \tilde{N}(z)$  for all  $i$ ; the inclusion of any information from the photometry would only introduce noise to the optimal result of returning the prior. This is the exact estimator, `trainZ`, that we have described in Section 3.3, and which will serve as an experimental control.

### A1 Metrics of the stacked estimator of the redshift distribution

Though alternatives exist ([Malz & Hogg prep](#)), “stacking” according to

$$\hat{N}^H(z) \equiv \frac{1}{N_{tot}} \sum_i^{N_{tot}} \hat{p}_i^H(z) \quad (\text{A1})$$

is the most widely accepted method for obtaining  $\hat{N}^H(z)$  as an estimator of the redshift distribution from photo- $z$  PDFs derived by a method  $H$ . Though the use of the stacked estimator of the redshift distribution is not formally correct, we use it under the untested assumption that the response of our metrics of  $\hat{N}^H(z)$  will be analogous to the same metrics applied to a principled estimator of the redshift distribution.

As  $N(z)$  is itself a univariate PDF, we apply the metrics of the previous sections to it as well. We additionally calculate the first three moments

$$\langle z^m \rangle \equiv \int_{-\infty}^{\infty} z^m N(z) dz \quad (\text{A2})$$

of the estimated redshift distribution  $\hat{N}^H(z)$  for each code and compare them to the moments of the true redshift distribution  $\tilde{N}(z)$ . Under the assumption that the stacked estimator is unbiased, a superior method minimizes the difference between the true and estimated moments.

### A2 Performance on the stacked estimator of the redshift distribution

Figure A1 shows the stacked estimator  $\hat{N}(z)$  of the redshift distribution for each code compared to the true redshift distribution  $\tilde{N}(z)$ , where the stacked estimator has been smoothed for each code in the plot using a kernel density

estimate (KDE) with a bandwidth chosen by Scott's Rule (Scott 1992) in order to minimize visual differences in small-scale features; the quantitative statistics, however, are calculated using the empirical CDF which is not smoothed.

Many of the codes, including all the model-fitting approaches and **ANNz2**, **GPz**, **METAPhoR**, and **SkyNet** from the data-driven camp, overestimate the redshift density at  $z \sim 1.4$ . This behavior is a consequence of the 4000 Åbreak passing through the gap between the  $z$  and  $y$  filters, which induces a genuine discontinuity in the  $z-y$  colour as a function of redshift that can sway the photo- $z$  PDF estimates in the absence of bluer spectral features.

**ANNz2**, **GPz**, and **METAPhoR** feature exaggerated peaks and troughs relative to the training set, a potential sign of overtraining. Further investigation on overtraining is needed, if present this is an obstacle that may be overcome with adjustment of the implementation.

As expected, **trainZ** perfectly recovers the true redshift distribution: as the training sample is selected from the same underlying distribution as the test set, the redshift distributions are identical, up to Poisson fluctuations due to the finite number of sample galaxies. **CMNN** is also in excellent agreement for similar reasons: with a representative training sample of galaxies spanning the colour-space, the sum of the colour-matched neighbour redshifts should return the true redshift distribution. **FlexZBoost** and **TPZ** also perform superb recovery of the true redshift distribution, with only a slight deviation at  $z \sim 1.4$ . Our metrics, however, cannot discern whether these four approaches, as well as **Delight**, are spared the  $z \sim 1.4$  degeneracy in  $\hat{N}(z)$  because they have more effectively used information in the data or if the impact is simply washed out by the stacked estimator's effective average over the test set galaxy sample. See Appendix B for further discussion of the  $z \sim 1.4$  issue.

Figure A2 shows the quantitative Kolmogorov-Smirnov (KS), Cramer-Von Mises (CvM), and Anderson Darling (AD) test statistics for each of the codes for the  $\hat{N}(z)$  based measures. The horizontal lines show the the result of a bootstrap resampling of the training set using 30,000 samples for **trainZ**, representing a conservative idealized limit on expected performance for a modest-sized representative training set of galaxies, as mentioned in Section 5.1. The AD bootstrap statistic is elevated due to its sensitivity to the tails of distributions. The stacked estimators of the redshift distribution for **CMNN** and **trainZ** best estimate  $\hat{N}(z)$  under these metrics, whereas **EAZY**, **LePhare**, **METAPhoR**, and **SkyNet** underperform; **BPZ**, **GPz**, and **TPZ** are within a factor of two of the conservative limit for all statistics. It is unsurprising that **CMNN** scores well, as with a nearly complete and representative training set choosing neighbouring points in color/magnitude space to construct an estimator should lead to excellent agreement in the final  $\hat{N}(z)$ .

It is, however, surprising that **TPZ** does well on  $\hat{N}(z)$  given its poor performance on the ensemble photo- $z$  PDFs, especially knowing that **TPZ** was optimized for photo- $z$  PDF ensemble metrics rather than the stacked estimator of the redshift distribution. A possible explanation is the choice of smoothing parameter chosen during validation, which affects photo- $z$  PDF widths as well as overall redshift bias and could be modified to improve performance under the photo- $z$  PDF metrics.

The first three moments of the stacked  $\hat{N}(z)$  distribu-

**Table A1.** Moments of the stacked estimator  $\hat{N}(z)$  of the redshift distribution. Most of the codes considered recover the moments of  $\hat{N}(z)$

Moments of $\hat{N}(z)$			
Estimator	mean	variance	skewness
Empirical "truth"	0.701	0.630	0.671
<b>ANNz2</b>	0.702	0.625	0.653
<b>BPZ</b>	0.699	0.629	0.671
<b>Delight</b>	0.692	0.609	0.638
<b>EAZY</b>	0.681	0.595	0.619
<b>FlexZBoost</b>	0.694	0.610	0.631
<b>GPz</b>	0.696	0.615	0.639
<b>LePhare</b>	0.718	0.668	0.741
<b>METAPhoR</b>	0.705	0.628	0.657
<b>CMNN</b>	0.701	0.628	0.667
<b>SkyNet</b>	0.743	0.708	0.797
<b>TPZ</b>	0.700	0.619	0.643
<b>trainZ</b>	0.699	0.627	0.666

tion relative to the empirical estimate of the truth distribution are given in Table A1. Accuracy of the moments varies widely between codes, raising concerns about the propagation to cosmological analyses.

**SkyNet** exhibits redshift bias in Figure A1 and is a clear outlier in the first moment of  $\hat{N}(z)$  in Table A1. The **SkyNet** algorithm employs a random subsampling of the training set without testing that the subset is representative of the full population, and the implementation used here does not upweight rarer low- and high-redshift galaxies, as in Bonnett (2015), suggesting a possible cause that may be addressed in future work.

## APPENDIX B: Photo- $z$ POINT ESTIMATION AND METRICS

While this work assumes that science applications value the information of the full photo- $z$  PDF, we present conventional metrics of photo- $z$  point estimates as a quick and dirty visual diagnostic tool and to facilitate direct comparisons to historical studies.

### B1 Reduction of photo- $z$ PDFs to point estimates

Though we acknowledge that many of the codes can also return a native photo- $z$  point estimate, we put all codes on equal footing by considering two generic photo- $z$  point estimators, the mode  $z_{PEAK}$  and main-peak-mean  $z_{WEIGHT}$  (Dahlen et al. 2013), a weighted mean within the bounds of the main peak, as identified by the roots of  $p(z) - 0.05 \times z_{PEAK}$ . Though  $z_{WEIGHT}$  neglects information in a secondary peak of e. g. a bimodal distribution, it avoids the pitfall of reducing the photo- $z$  PDF to a redshift between peaks where there is low probability.

### B2 Metrics of photo- $z$ point estimates

We calculate the commonly used point estimate metrics of the overall intrinsic scatter, bias, and catastrophic outlier

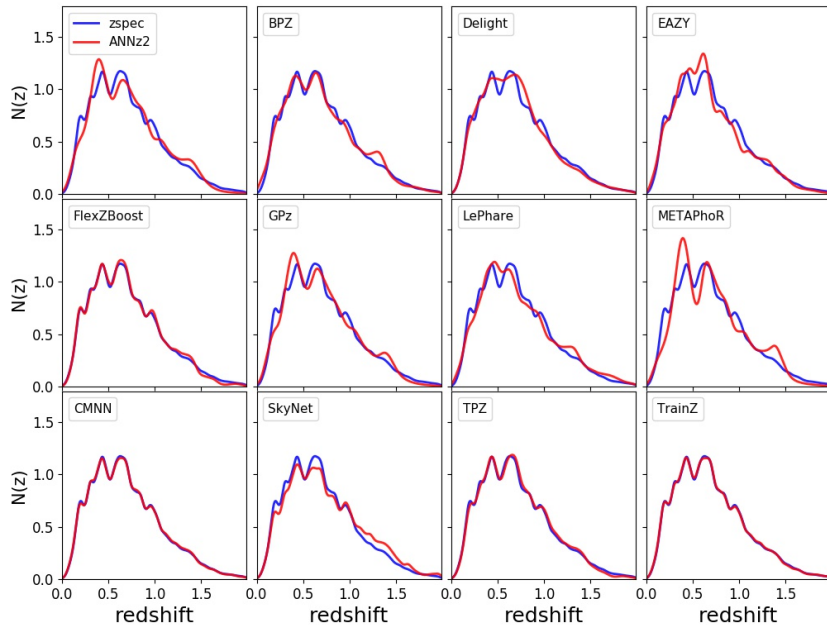


**Figure A1.** The smoothed stacked estimator  $\hat{N}(z)$  of the redshift distribution (red) produced by each code (panels) compared to the true redshift distribution  $\tilde{N}(z)$  (blue). Varying levels of agreement are seen among the codes, with the smallest deviations for CMNN, FlexZBoost, TPZ, and trainZ.

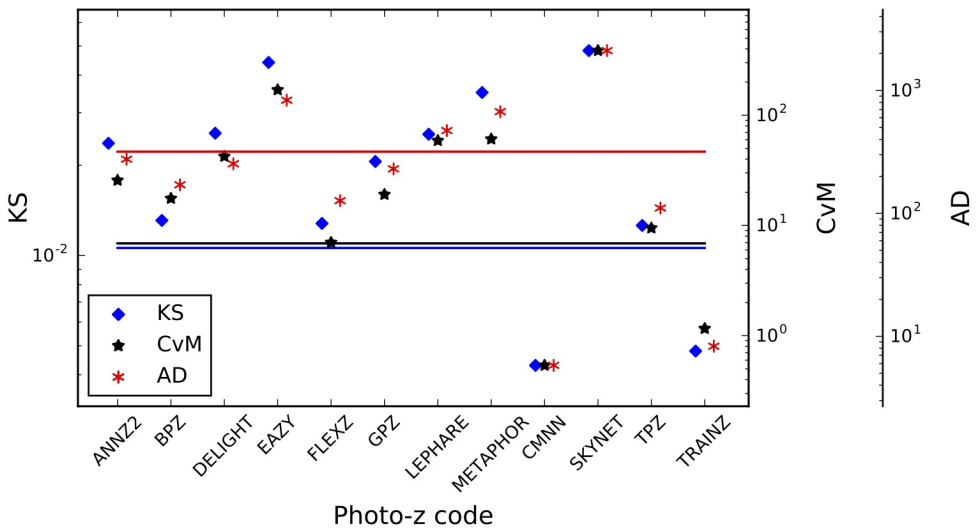


**Figure A2.** A visualization of the Kolmogorov-Smirnov (KS, blue diamond), Cramer-von Mises (CvM, black star), and Anderson-Darling (AD, red asterisk) statistics for the  $\hat{N}(z)$  distributions. Horizontal lines indicate the statistic values (including uncertainty) achieved using trainZ via bootstrap resampling a training set containing 30,000 redshifts. We make the reassuring observation that these related statistics do not disagree significantly with one another. CMNN outperforms the control case, trainZ, and several codes are within a factor of two of this conservative idealized limit. SKYNET scores poorly due to an overall bias in its redshift predictions.

rate, defined in terms of the standard error  $e_z \equiv (z_{PEAK} - z_{true})/(1 + z_{true})$ . Because the standard deviation of the photo-z residuals is sensitive to outliers, we define the scatter in terms of the Interquartile Range (IQR), the difference between the 75th and 25th percentiles of the distribution of  $e_z$ , imposing the scaling  $\sigma_{IQR} = IQR/1.349$  to ensure that the area within  $\sigma_{IQR}$  is the same as that within one standard deviation from a standard Normal distribution. We also resist the effect of catastrophic outliers by defining the bias  $b_z$  as the median rather than mean value of  $e_z$ . The cata-

- trophic outlier rate  $f_{\text{out}}$  is defined as the fraction of galaxies with  $e_z$  greater than  $\max(3\sigma_{\text{IQR}}, 0.06)$ .<sup>18</sup>
- For reference, Section 3.8 of the LSST Science Book (Abell et al. 2009) uses the standard definitions of these parameters in requiring
- RMS scatter  $\sigma < 0.02(1 + z_{\text{true}})$
  - bias  $b_z < 0.003$
  - catastrophic outlier rate  $f_{\text{out}} < 10\%$ .
- ### B3 Comparison of photo- $z$ point estimate metrics
- Figure B1 shows both point estimates for all codes both  $z_{\text{PEAK}}$  and  $z_{\text{WEIGHT}}$ . Point density is shown with mixed contours to emphasize that most of the galaxies do fall close to the  $z_{\text{phot}} = z_{\text{spec}}$  line, while points trace the details of the catastrophic outlier populations.
- The finite grid spacing of the photo- $z$  PDFs induces some discretization in  $z_{\text{PEAK}}$ . The features perpendicular to the  $z_{\text{phot}} = z_{\text{spec}}$  line are due to the 4000 Åbreak passing through the gaps between adjacent filters. Even the strongest codes feature populations far from the  $z_{\text{phot}} = z_{\text{spec}}$  line representing a degeneracy in the space of colours and redshifts.
- The intrinsic scatter, bias, and catastrophic outlier rate are given in Table B1. Perhaps unsurprisingly, performance under these metrics largely tracks that of the metrics of Section 4 of the photo- $z$  PDFs from which the point estimates were derived. All twelve codes perform at or near the goals of the LSST Science Requirements Document<sup>18</sup> and Graham et al. (2018), which is encouraging if not unexpected for  $i < 25.3$ .
- ## REFERENCES
- Abbott T., et al., 2005, preprint (arXiv:astro-ph/0510346)  
 Abell P. A., et al., 2009, preprint (arXiv:0912.0201),  
 Aihara H., et al., 2018a, *PASJ*, **70**, S4  
 Aihara H., et al., 2018b, *PASJ*, **70**, S8  
 Almosallam I. A., Lindsay S. N., Jarvis M. J., Roberts S. J., 2016a, *MNRAS*, **455**, 2387  
 Almosallam I. A., Jarvis M. J., Roberts S. J., 2016b, *MNRAS*, **462**, 726  
 Arnouts S., Cristiani S., Moscardini L., Matarrese S., Lucchin F., Fontana A., Giallongo E., 1999, *MNRAS*, **310**, 540  
 Behroozi P. S., Wechsler R. H., Wu H.-Y., 2013, *ApJ*, **762**, 109  
 Benítez N., 2000, *ApJ*, **536**, 571  
 Bernstein G., Huterer D., 2010, *MNRAS*, **401**, 1399  
 Blanton M. R., Roweis S., 2007, *AJ*, **133**, 734  
 Blanton M. R., et al., 2005, *AJ*, **129**, 2562  
 Bonnett C., 2015, *MNRAS*, **449**, 1043  
 Bonnett C., 2016, Python wrapper to SkyNet, <https://pyskynet.readthedocs.io/en/latest/>  
 Bonnett C., et al., 2016, *Phys. Rev. D*, **94**, 042005  
 Bordoloi R., Lilly S. J., Amara A., 2010, *MNRAS*, **406**, 881  
 Brammer G. B., van Dokkum P. G., Coppi P., 2008, *ApJ*, **686**, 1503  
 Breiman L., Friedman J. H., Olshen R. A., Stone C. J., 1984, Classification and Regression Trees, Statistics/Probability Series, Wadsworth Publishing Company, Belmont, California, U.S.A.  
 Brescia M., Cavuoti S., Amaro V., Riccio G., Angora G., Vellucci C., Longo G., 2018, preprint, ([arXiv:1802.07683](https://arxiv.org/abs/1802.07683))  
 Carrasco Kind M., Brunner R. J., 2013, *MNRAS*, **432**, 1483  
 Carrasco Kind M., Brunner R. J., 2014, *MNRAS*, **442**, 3380  
 Cavuoti S., Amaro V., Brescia M., Vellucci C., Tortora C., Longo G., 2017, *MNRAS*, **465**, 1959  
 Chen T., Guestrin C., 2016, in Proceedings of the 22Nd ACM SIGKDD International Conference on Knowledge Discovery and Data Mining, KDD '16. ACM, New York, NY, USA, pp 785–794, doi:[10.1145/2939672.2939785](https://doi.acm.org/10.1145/2939672.2939785), <http://doi.acm.org/10.1145/2939672.2939785>  
 Connolly A. J., et al., 2014, in Angeli G. Z., Dierickx P., eds, Society of Photo-Optical Instrumentation Engineers (SPIE) Conference Series Vol. 9150, Modeling, Systems Engineering, and Project Management for Astronomy VI. p. 14, doi:[10.1117/12.2054953](https://doi.org/10.1117/12.2054953)  
 Dahlen T., et al., 2013, *ApJ*, **775**, 93  
 Dawson W. A., Schneider M. D., Tyson J. A., Jee M. J., 2016, *ApJ*, **816**, 11  
 DeRose J., et al., 2019, arXiv e-prints, p. [arXiv:1901.02401](https://arxiv.org/abs/1901.02401)  
 Erben T., et al., 2013, *MNRAS*, **433**, 2545  
 Fernández-Soto A., Lanzetta K. M., Yahil A., 1999, *ApJ*, **513**, 34  
 Firth A. E., Lahav O., Somerville R. S., 2003, *MNRAS*, **339**, 1195  
 Freeman P. E., Izbicki R., Lee A. B., 2017, *MNRAS*, **468**, 4556  
 Graff P., Feroz F., Hobson M. P., Lasenby A., 2014, *MNRAS*, **441**, 1741  
 Graham M. L., Connolly A. J., Ivezić Ž., Schmidt S. J., Jones R. L., Jurić M., Daniel S. F., Yoachim P., 2018, *AJ*, **155**, 1  
 Green J., et al., 2012, preprint (arXiv:1208.4012),  
 Hildebrandt H., et al., 2010, *A&A*, **523**, A31  
 Hofmann B., Mathé P., 2018, *Inverse Problems*, **34**, 015007  
 Hunter J. D., 2007, Matplotlib: A 2D Graphics Environment, doi:[10.1109/MCSE.2007.55](https://doi.org/10.1109/MCSE.2007.55)  
 Ilbert O., et al., 2006, *A&A*, **457**, 841  
 Ivezić Ž., et al., 2008, preprint (arXiv:0805.2366),  
 Izbicki R., Lee A. B., 2017, *Electron. J. Statist.*, **11**, 2800  
 Izbicki R., Lee A. B., Freeman P. E., 2017, *Ann. Appl. Stat.*, **11**, 698  
 Laureijs R., et al., 2011, preprint (1110.3193),  
 Leistedt B., Hogg D. W., 2017, *ApJ*, **838**, 5  
 Malz A., Hogg D., in prep., CHIPPR, chippr, <https://github.com/aimalz/chippr>  
 Malz A., Marshall P., 2018, qp: Quantile parametrization for probability distribution functions (ascl:1809.011)  
 Malz A. I., Marshall P. J., DeRose J., Graham M. L., Schmidt S. J., Wechsler R., (LSST Dark Energy Science Collaboration 2018, *AJ*, **156**, 35)  
 Mandelbaum R., et al., 2008, *MNRAS*, **386**, 781  
 Massarotti M., Iovino A., Buzzoni A., 2001, *A&A*, **368**, 74  
 Masters D. C., Stern D. K., Cohen J. G., Capak P. L., Rhodes J. D., Castander F. J., Paltoni S., 2017, *ApJ*, **841**, 111  
 Newman J. A., et al., 2015, *Astroparticle Physics*, **63**, 81  
 Oliphant T., 2007, Python for Scientific Computing, doi:[10.1109/MCSE.2007.55](https://doi.org/10.1109/MCSE.2007.55)  
 Oyaizu H., Lima M., Cunha C. E., Lin H., Frieman J., 2008, *ApJ*, **689**, 709  
 Polsterer K. L., D’Isanto A., Gieseke F., 2016, preprint (arXiv:1608.08016),  
 Rasmussen C., Williams C., 2006, Gaussian Processes for Machine Learning. Adaptative computation and machine learning series, MIT Press, Cambridge, MA  
 Rau M. M., Seitz S., Brimoulle F., Frank E., Friedrich O., Gruen D., Hoyle B., 2015, *MNRAS*, **452**, 3710  
 Reddick R. M., Wechsler R. H., Tinker J. L., Behroozi P. S., 2013, *ApJ*, **771**, 30  
 Sadeh I., Abdalla F. B., Lahav O., 2016, *PASP*, **128**, 104502  
 Sánchez C., et al., 2014, *MNRAS*, **445**, 1482  
 Schmidt M., 2005, minFunc: Unconstrained Differentiable Mul-

<sup>18</sup> available at: <http://ls.st/srd>

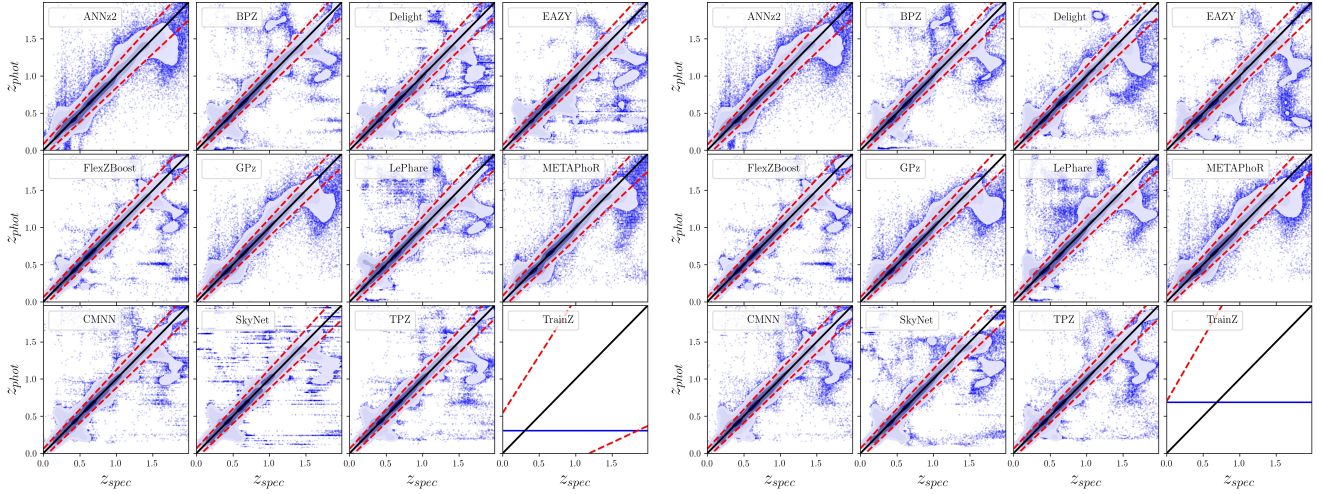


**Figure B1.** The density of photo- $z$  point estimates (contours) reduced from the photo- $z$  PDFs with outliers (blue) beyond the outlier cutoff (red dashed lines), via the mode ( $z_{PEAK}$ , left panel) and main-peak-mean ( $z_{WEIGHT}$ , right panel). The **trainZ** estimator (lower right sub-panels) has a shared  $z_{PEAK}$  and  $z_{WEIGHT}$  for the entire test set galaxy sample.

**Table B1.** Photo- $z$  point estimate statistics

Photo- $z$ PDF Code	$Z_{PEAK}$		$Z_{WEIGHT}$			
	$\sigma_{IQR}/(1+z)$	median	outlier fraction	$\sigma_{IQR}/(1+z)$	median	outlier fraction
ANNz2	0.0270	0.00063	0.044	0.0244	0.000307	0.047
BPZ	0.0215	-0.00175	0.035	0.0215	-0.002005	0.032
Delight	0.0212	-0.00185	0.038	0.0216	-0.002158	0.038
EAZY	0.0225	-0.00218	0.034	0.0226	-0.003765	0.029
FlexZBoost	0.0154	-0.00027	0.020	0.0148	-0.000211	0.017
GPz	0.0197	-0.00000	0.052	0.0195	0.000113	0.051
LePhare	0.0236	-0.00161	0.058	0.0239	-0.002007	0.056
METAPhoR	0.0264	0.00000	0.037	0.0262	0.001333	0.048
CMNN	0.0184	-0.00132	0.035	0.0170	-0.001049	0.034
SkyNet	0.0219	-0.00167	0.036	0.0218	0.000174	0.037
TPZ	0.0161	0.00309	0.033	0.0166	0.003048	0.031
<b>trainZ</b>	0.1808	-0.2086	0.000	0.2335	0.022135	0.000

- 1510 tivariate Optimization in Matlab, <http://www.cs.ubc.ca/~schmidtm/Software/minFunc.html>  
 1511  
 1512 Scott D. W., 1992, Multivariate Density Estimation. Theory,  
 1513 Practice, and Visualization. Wiley  
 1514 Sheldon E. S., Cunha C. E., Mandelbaum R., Brinkmann J.,  
 1515 Weaver B. A., 2012, *The Astrophysical Journal Supplement  
 Series*, 201, 32  
 1516 Skrutskie M. F., et al., 2006, AJ, 131, 1163  
 1517 Tanaka M., et al., 2018, PASJ, 70, S9  
 1518 The LSST Dark Energy Science Collaboration et al., 2018,  
 1519 preprint, ([arXiv:1809.01669](https://arxiv.org/abs/1809.01669))  
 1520 Waskom M., et al., 2017, doi:10.5281/zenodo.824567  
 1521 York D. G., et al., 2000, AJ, 120, 1579  
 1522 de Jong J. T. A., Verdoes Kleijn G. A., Kuijken K. H., Valentijn  
 1523 E. A., 2013, *Exp. Astron.*, 35, 25  
 1524 de Jong J. T. A., et al., 2017, A&A, 604, A134